

NUMERICAL SIMULATIONS OF FLARE-PRODUCTIVE ACTIVE REGIONS: δ -SUNSPOTS, SHEARED
POLARITY INVERSION LINES, ENERGY STORAGE, AND PREDICTIONS

SHIN TORIUMI¹

SHINSUKE TAKASAO²

¹*National Astronomical Observatory of Japan, 2-21-1 Osawa, Mitaka, Tokyo 181-8588, Japan*

²*Department of Physics, Nagoya University, Furo-cho, Chikusa-ku, Nagoya, 464-8602 Aichi, Japan*

(Received; Revised; Accepted)

Submitted to ApJ

ABSTRACT

Solar active regions (ARs) that produce strong flares and coronal mass ejections (CMEs) are known to have a relatively high non-potentiality and are characterized by δ -sunspots and sheared magnetic structures. In this study, we conduct a series of flux emergence simulations from the convection zone to the corona and model four types of active regions that have been observationally suggested to cause strong flares, namely the Spot-Spot, Spot-Satellite, Quadrupole, and Inter-AR cases. As a result, we confirm that δ -spot formation is due to the complex geometry and interaction of emerging magnetic fields, with finding that the strong-field, high-gradient, highly-sheared polarity inversion line (PIL) is created by the combined effect of the advection, stretching, and compression of magnetic fields. We show that free magnetic energy builds up in the form of a current sheet above the PIL. It is also revealed that photospheric magnetic parameters that predict flare eruptions reflect the stored free energy with high accuracy, while CME-predicting parameters indicate the magnetic relationship between flaring zones and entire ARs.

Keywords: Sun: corona — Sun: flares — Sun: interior — Sun: photosphere — (Sun:) sunspots

arXiv:1710.08926v1 [astro-ph.SR] 24 Oct 2017

1. INTRODUCTION

Strong flares and coronal mass ejections (CMEs), the most catastrophic energy-releasing events in the solar system, are known to occur in active regions (ARs) including sunspots (Priest & Forbes 2002; Shibata & Magara 2011). Numerous observations have revealed that complex ARs called “ δ -sunspots,” in which the umbrae of positive and negative polarities share a common penumbra, tend to produce powerful flare eruptions (Künzel 1960)¹. According to statistical studies by Shi & Wang (1994), Sammis et al. (2000), and Guo et al. (2014), more than 80% of *GOES* X-class flares occur in δ -spots. In such ARs, flare eruptions often occur in sheared magnetic structures above polarity inversion lines (PILs). Many observers have pointed out the importance of strong-field, high-gradient, highly-sheared PILs (e.g., Haggard et al. 1984; Tanaka 1991; Zirin & Wang 1993; Falconer et al. 2002; Schrijver 2007). Therefore, for understanding flare eruptions, it is essential to reveal the formation of δ -spots and such sheared structures and its relation with the evolution of entire ARs (for further review see Wang & Liu 2015).

Recently, Toriumi et al. (2017) surveyed all ARs that produced \geq M5.0-class events in Solar Cycle 24 (events within 45° from the disk center in 6 yr from May 2010) and classified them into four categories based on pioneering work by Zirin & Liggett (1987): see also Takizawa & Kitai (2015). Figure 1 summarizes the four categories.

Spot-Spot: A complex, compact δ -spot group, in which a large, long sheared PIL extends across the whole AR. A representative region is NOAA AR 11429, which produced an X5.4-class event along the central PIL. Takasao et al. (2015) suggested the possibility that this AR is created through the emergence of a strongly twisted, kink unstable flux tube (see also Tanaka 1991; Linton et al. 1996; Fan et al. 1999).

Spot-Satellite: A newly emerging minor bipole appears in the close vicinity of one of the preexisting main sunspots and creates a small δ -spot with a compact PIL between the main and satellite spots. NOAA 12017, producing an X1.0 event, falls into this category (Kleint et al. 2015).

Quadrupole: A δ -configuration is formed by the collision of opposite polarities from two emerging

bipoles of comparable size. A typical example is NOAA 11158, in which a series of strong flares emanated from its central PIL (Schrijver et al. 2011). Toriumi et al. (2014) and Fang & Fan (2015) suggested that this AR is created by the emergence of a single flux tube that rises at two locations.

Inter-AR: Strong flares produced on the PIL between two separated, apparently independent ARs. They show no clear δ -configuration nor a clear sheared PIL at the flaring sites. The X1.2-class flare that occurred between NOAA ARs 11944 and 11943 is a representative event of this category. It produced a very fast CME ($\sim 2,400$ km s⁻¹) that could potentially cause a severe geomagnetic disturbance (Möstl et al. 2015; Wang et al. 2015).

The creation of non-potential structures such as δ -spots and sheared PILs is a result of large-scale flux emergence from the solar interior and eventual sunspot motions. In this paper, in order to investigate the formation of the four above-mentioned types of ARs that can potentially produce flares, CMEs, and perhaps Earth-affecting disturbances, we conduct a series of flux emergence simulations. While flux emergence occurs as a result of the dynamo mechanism acting inside the Sun (Parker 1955), here we focus more on the complexity and interaction of magnetic flux systems rising in the interior and the resultant formation of ARs.

Flux emergence simulations from the convection zone have widely been used to model solar ARs in the last two decades (e.g., Fan 2001; Archontis et al. 2004; Cheung et al. 2010; Toriumi & Yokoyama 2011, 2012; Rempel & Cheung 2014; for review see Cheung & Isobe 2014). In the present work, we test four different flux emergence simulations, including those suggested previously to model δ -spots (Fan et al. 1999; Toriumi et al. 2014; Fang & Fan 2015; Takasao et al. 2015), using similar numerical conditions, and explore, in particular, the formation of δ -spots with sheared PILs in the surface layer as well as the buildup of free magnetic energy in the atmosphere.

Thanks to recent progress in accurate magnetic measurements and high-performance computations, several flare and CME prediction methods have been suggested and developed (e.g., Leka & Barnes 2003; Schrijver 2007; Welsch et al. 2009; Fisher et al. 2012). Bobra & Couvidat (2015) extracted various photospheric parameters from vector magnetograms (SHARP parameters) and obtained good predictive performance for \geq M1.0 flares using a machine learning algorithm. In this paper, we utilize a series of numerical simulations, which reproduce flaring ARs with non-potential

¹ The other classifications of the Mount Wilson magnetic classification are α (unipole), β (bipole), and γ (multiple spots with intermixed polarity).

structures (δ -spots and sheared PILs), to examine why these photospheric parameters predict flare events that occur in the corona with higher accuracy.

The rest of the paper is organized as follows. In Section 2, we describe the numerical setup and assumed conditions for the four simulation cases. Then, in Section 3, the general evolution of the four cases is shown. Sections 4 and 5 are dedicated to presenting the detailed development of δ -spots and sheared PILs in the photosphere and the coronal energy buildup, respectively, while Section 6 explores the prediction of flares and CMEs using photospheric parameters. We summarize and discuss the results in Sections 7 and 8, respectively.

2. NUMERICAL SETUP

2.1. Assumptions and Basic Equations

In this paper, we investigated the emergence of buoyant flux tubes initially set in the convection zone. We considered a rectangular computational domain with three-dimensional (3D) Cartesian coordinates (x, y, z) , where the z -coordinate increases upward. We solved the standard set of resistive magnetohydrodynamic (MHD) equations:

$$\frac{\partial \rho}{\partial t} + \nabla \cdot (\rho \mathbf{V}) = 0, \quad (1)$$

$$\frac{\partial}{\partial t}(\rho \mathbf{V}) - \nabla \cdot \left[\rho \mathbf{V} \mathbf{V} + \left(p + \frac{\mathbf{B}^2}{8\pi} \right) \mathbf{I} - \frac{\mathbf{B} \mathbf{B}}{4\pi} \right] + \rho \mathbf{g} = 0, \quad (2)$$

$$\frac{\partial \mathbf{B}}{\partial t} = c \nabla \times \mathbf{E}, \quad (3)$$

$$\begin{aligned} & \frac{\partial}{\partial t} \left(\rho U + \frac{1}{2} \rho \mathbf{V}^2 + \frac{\mathbf{B}^2}{8\pi} \right) \\ & + \nabla \cdot \left[\left(\rho U + p + \frac{1}{2} \rho \mathbf{V}^2 \right) \mathbf{V} + \frac{c}{4\pi} \mathbf{E} \times \mathbf{B} \right] \\ & - \rho \mathbf{g} \cdot \mathbf{V} = 0, \end{aligned} \quad (4)$$

and

$$U = \frac{1}{\gamma - 1} \frac{p}{\rho}, \quad (5)$$

$$\mathbf{E} = -\frac{1}{c} \mathbf{V} \times \mathbf{B} + \eta \mathbf{J}, \quad (6)$$

$$\mathbf{J} = \frac{c}{4\pi} \nabla \times \mathbf{B}, \quad (7)$$

$$p = \frac{k_B}{m} \rho T, \quad (8)$$

where ρ denotes the gas density, \mathbf{V} velocity vector, p pressure, \mathbf{B} magnetic field, c the speed of light, \mathbf{E} electric field, and T temperature, while U is the internal energy per unit mass, \mathbf{I} the unit tensor, k_B the Boltzmann constant, m ($= \text{const.}$) the mean molecular mass, and $\mathbf{g} = (0, 0, -g_0) = (0, 0, -1/\gamma)$ the uniform gravitational acceleration. We assumed the medium to be an inviscid perfect gas with a specific heat ratio $\gamma = 5/3$.

To make the above equations dimensionless, we introduced the following normalizing units: the pressure scale height $H_0 = 170$ km for length, the sound speed $C_{s0} = 6.8$ km s⁻¹ for velocity, $\tau_0 \equiv H_0/C_{s0} = 25$ s for time, and $\rho_0 = 1.4 \times 10^{-7}$ g cm⁻³ for density, all of which are typical values in the photosphere. The gas pressure, temperature, and magnetic field strength were normalized by the combinations of the units above, i.e., $p_0 = \rho C_{s0}^2 = 6.3 \times 10^4$ dyn cm⁻², $T_0 = m C_{s0}^2 / (\gamma k_B) = 5,600$ K, and $B_0 = (\rho_0 C_{s0}^2)^{1/2} = 250$ G, respectively.

We assumed an anomalous resistivity model with the form

$$\eta = \begin{cases} 0 & (J < J_C \text{ or } \rho > \rho_C) \\ \eta_0 (J/J_C - 1) & (J \geq J_C \text{ and } \rho < \rho_C) \end{cases}, \quad (9)$$

where $\eta_0 = 0.1$, $J_C = 0.1$, and $\rho_C = 0.1$. The above treatment is intended to trigger magnetic reconnection in a low-density current sheet.

2.2. Numerical Conditions and the Reference Case

The initial background atmosphere consisted of three regions: an adiabatically stratified convection zone, a cool isothermal photosphere/chromosphere, and a hot isothermal corona (see Figure 2). We assumed $z/H_0 = 0$ to be the base height of the photosphere, and the initial temperature distribution of the convection zone ($z/H_0 \leq 0$) was assumed to be

$$T(z) = T_{\text{ph}} - z \left| \frac{dT}{dz} \right|_{\text{ad}}, \quad (10)$$

where $T_{\text{ph}} = T_0$ is the photospheric temperature and

$$\left| \frac{dT}{dz} \right|_{\text{ad}} = \frac{\gamma - 1}{\gamma} \frac{m g_0}{k_B} \quad (11)$$

is the adiabatic temperature gradient; i.e., the initial temperature profile of the convection zone is adiabatic. The temperature distribution of the atmosphere ($z/H_0 \geq 0$) was expressed as

$$T(z) = T_{\text{ph}} + \frac{1}{2} (T_{\text{cor}} - T_{\text{ph}}) \left[\tanh \left(\frac{z - z_{\text{cor}}}{w_{\text{tr}}} \right) + 1 \right], \quad (12)$$

where $T_{\text{cor}} = 150T_0$ is the coronal temperature, $z_{\text{cor}} = 18H_0$ is the base of the corona, and $w_{\text{tr}} = 2H_0$ is the temperature scale height of the transition region. With the temperature profile above, the initial pressure and density profiles (Figure 2) were defined by the equation of static pressure balance:

$$\frac{dp(z)}{dz} + \rho(z)g_0 = 0. \quad (13)$$

A magnetic flux tube was embedded in the convection zone and its longitudinal and azimuthal components of the flux tube are given by

$$B_x(r) = B_{\text{tube}} \exp\left(-\frac{r^2}{R_{\text{tube}}^2}\right) \quad (14)$$

and

$$B_\phi = qrB_x(r), \quad (15)$$

where $r = [(y - y_{\text{tube}})^2 + (z - z_{\text{tube}}^2)]^{1/2}$ is the radial distance from the tube axis, $(y_{\text{tube}}, z_{\text{tube}})$ the location of the tube axis, R_{tube} the radius, B_{tube} the magnetic field strength at the axis, and q the twist intensity. As the Reference (typical) case, we considered $(y_{\text{tube}}/H_0, z_{\text{tube}}/H_0) = (0, -30)$, $R_{\text{tube}}/H_0 = 3$, $B_{\text{tube}}/B_0 = 30$, and $qH_0 = -0.2$. The total axial magnetic flux amounts to $\Phi_{\text{tube}}/(B_0H_0^2) = 845$. These parameters indicate that the initial flux tube is located at a depth of 5.1 Mm and has a radius of 510 km; a central field strength of 7.5 kG (or the plasma $\beta \equiv 8\pi p/B^2 \sim 10$), which yields an axial flux of 6×10^{19} Mx; and a left-handed twist. The magnetic pressure, $p_{\text{mag}} = B^2/(8\pi)$, along the vertical axis is shown in Figure 2. The gas pressure inside the tube was defined as $p_i = p(z) + \delta p_{\text{exc}}$, with the pressure excess being

$$\delta p_{\text{exc}} = \frac{B_x^2(r)}{8\pi} \left[q^2 \left(\frac{R_{\text{tube}}^2}{2} - r^2 \right) - 1 \right] (< 0). \quad (16)$$

To trigger the buoyant emergence, we reduced the density inside the flux tube, $\rho_i = \rho(z) + \delta\rho_{\text{exc}}$, where

$$\delta\rho_{\text{exc}} = \rho(z) \frac{\delta p_{\text{exc}}}{p(z)} \left[(1 + \epsilon) \exp\left(-\frac{(x - x_{\text{tube}})^2}{\lambda^2}\right) - \epsilon \right] \quad (17)$$

and x_{tube} and λ are the center and the length of the buoyant section, respectively, and ϵ is a factor that suppresses the emergence of both ends of the tube. The typical values are $x_{\text{tube}}/H_0 = 0$, $\lambda/H_0 = 8$, and $\epsilon = 0.2$. Depending on the simulation case, some parameters were modified as described in the next subsection.

The simulation domain was $(-150, -150, -40) \leq (x/H_0, y/H_0, z/H_0) \leq (150, 150, 400)$, resolved by a

$512 \times 512 \times 512$ grid. The grid spacings for the x -, y -, and z -directions were $\Delta x/H_0 = \Delta y/H_0 = 0.25$ for $(-20, -20) \leq (x/H_0, y/H_0) \leq (20, 20)$ and $\Delta z/H_0 = 0.2$ for $-40 \leq z/H_0 \leq 15$. Outside this range, the spacings were smoothly increased up to $\Delta x/H_0 = \Delta y/H_0 = 0.8$ and $\Delta z/H_0 = 1.8$. We assumed a periodic boundary condition for the x -direction and symmetric boundaries for both the y - and z -directions.

The simulation code we used is the same as that used by Takasao et al. (2015), which is based on the numerical scheme of Vögler et al. (2005): 4th-order central differences for calculating the spatial derivatives and the four-step Runge-Kutta scheme for calculating the temporal derivatives. Artificial diffusivity, proposed by Rempel et al. (2009), was introduced to stabilize the calculation, while the $\nabla \cdot \mathbf{B}$ error was reduced by the iterative hyperbolic divergence cleaning technique based on the method described in Dedner et al. (2002).

Figure 3 shows the evolution of the magnetogram at $z/H_0 = 0$ and magnetic field lines for the Reference case (movie is attached to provide detailed evolution). The whole evolution is consistent with the previous 3D simulations by, e.g., Fan (2001), Archontis et al. (2004), and Toriumi & Yokoyama (2012): the horizontal flux tube makes an Ω -shaped arcade, which rises through the convection zone and eventually penetrate the photosphere, creating a magnetic dome in the corona with bipolar spots in the photosphere.

2.3. Four Simulation Cases

In order to model the four types of flare-productive ARs introduced in Section 1, we tested four simulation cases with initial conditions different from those of the Reference case, which are summarized in the bottom row of Figure 1.

For the Spot-Spot case, the initial twist strength was intensified to $qH_0 = -0.8$, which is larger than the critical value for the kink instability ($|q|H_0 = 0.33$: Linton et al. 1996). Due to the stronger initial twist, the density deficit is larger for this case (Equations (16) and (17)) and thus the flux tube starts with a faster rising speed (see, e.g., Murray et al. 2006). At the same time, the kinking itself accelerates the flux tube: When the tube kinks, its axis is stretched, which enhances the buoyancy and makes the rise speed faster (Fan et al. 1999).

The second case, Spot-Satellite, was modeled by introducing a parasitic flux tube set in a direction perpendicular to the main flux tube. Perhaps this type can also be produced from a single flux tube that bifurcates. However, in this paper, for simplicity, we tested the two-tube scenario (main and parasitic tubes).

The parasitic tube has parameters of $R_{\text{tube}}/H_0 = 2$, $B_{\text{tube}}/B_0 = 15$, and $qH_0 = -0.2$ (directed to $+y$ with a left-handed twist). The tube center is located at $(x/H_0, y/H_0, z/H_0) = (15, 0, -14)$ and is kept in mechanical balance. In this model, a periodic boundary condition was applied in the y -direction.

The Quadrupole flux tube has two buoyant sections along the axis and thus starts emergence at two locations. We changed the density perturbation of Equation (17) to

$$\delta\rho_{\text{exc}} = \rho(z) \frac{\delta p_{\text{exc}}}{p(z)} \left[(1 + \epsilon) \exp\left(-\frac{(x - x_{\text{tube1}})^2}{\lambda^2}\right) + (1 + \epsilon) \exp\left(-\frac{(x - x_{\text{tube2}})^2}{\lambda^2}\right) - \epsilon \right] \quad (18)$$

where $x_{\text{tube1}}/H_0 = -3\lambda/H_0 = -24$ and $x_{\text{tube2}}/H_0 = 3\lambda/H_0 = 24$.

Finally, for the Inter-AR case, we set two flux tubes in parallel in the convection zone. The two tubes have parameters of $(x_{\text{tube1}}/H_0, y_{\text{tube1}}/H_0) = (3\lambda/H_0, -3\lambda/H_0) = (24, -24)$ and $(x_{\text{tube2}}/H_0, y_{\text{tube2}}/H_0) = (-3\lambda/H_0, 3\lambda/H_0) = (-24, 24)$.

In this work, for the purposes of comparing the simulations to observations, we refer to the emerged region as δ -spots if it is complex (qualitatively), compact (separation of the both polarities less than, say, $20H_0$), and highly sheared (shear angle of the PIL $\sim 90^\circ$). Note that we take these values for just a threshold in the simulations and they are not actually measured from observations. Also, although previous observations found that the δ -spots often show rotational motions and violate Hale's polarity rule (e.g. Kurokawa 1987; López Fuentes et al. 2000, 2003), these properties are not used as the definition here.

3. GENERAL EVOLUTION

Figures 4, 5, 6, and 7 are the photospheric magnetograms and field lines for the Spot-Spot, Spot-Satellite, Quadrupole, and Inter-AR cases, respectively, while Figure 8 compares the apex heights, z/H_0 , as a function of t/τ_0 and the surface total unsigned magnetic flux, $\Phi = \int |B_z| dx dy$, since the flux appears at the surface. From these diagrams, one can observe that the most drastic evolution is for the Spot-Spot case, i.e., the emergence of a highly-twisted kink-unstable flux tube. As explained in detail in earlier works by Fan et al. (1999) and Takasao et al. (2015), this flux tube quickly develops a knotted structure in the convection zone rather than making a simple Ω -shaped arch (see field line rendering at $t/\tau_0 = 50$), reducing its twist about the axis by making the axis writhed. It reaches the surface around $t/\tau_0 = 75$ with the orientation of the axis that con-

nects the two main surface polarities highly deviated from the direction of the original flux tube (see magnetogram at $t/\tau_0 = 100$); i.e., this AR violates Hale's polarity rule. Eventually, at $t/\tau_0 = 300$, the magnetogram shows a pair of circular spots of opposite polarities around $(x/H_0, y/H_0) = (\pm 45, \pm 5)$ with extended tails. An elongated PIL is built in the middle of the domain, sandwiched by the two main sunspots. The total magnetic flux at the surface is more than 10 times the original axial flux. This is mostly because the original flux tube has a strong twist and thus a large amount of azimuthal flux in addition to the axial component, but this is also because some field lines wander up and down the surface layer, which increases the total unsigned flux. Since this AR is composed of bipolar spots with scattered patches and closely-neighboring opposite polarities, it can be classified as a $\beta\gamma\delta$ spot.

The remaining three cases show relatively gentle evolutions. For the Spot-Satellite case (Figure 5), the rising Ω -shaped main tube comes into contact with the resting parasitic tube at $t/\tau_0 = 150$ and starts pushing it up. From $t/\tau_0 = 200$, the surface magnetogram shows a separation of the main bipolar spots in the x -direction, with minor satellite spots separating along the y -axis at $x/H_0 \sim 25$ (see green arrows in the magnetogram). A compact PIL is formed between the negative main spot and the positive satellite polarity only for a short period when the positive polarity transits alongside the negative spot and forms a δ -spot structure. In the corona, field lines of the parasitic tube (green lines in field line rendering) are pushed aside along the positive x -direction by the main flux tube (yellow lines). Owing to magnetic reconnection, some green field lines trace the original tube in the convection zone deeper down to both footpoints. The final surface flux is slightly larger than twice the original axial flux, probably because of the contribution of the satellite spots (Figure 8). We conjecture that this AR can also be a $\beta\gamma\delta$ spot.

The two density-deficit sections along the flux tube of the Quadrupole case create an M-shaped configuration in the convection zone (Figure 6). The rising speed in the interior is approximately the same as that of the Spot-Satellite case. From $t/\tau_0 = 200$, the flux tube creates a pair of bipoles at the surface, and from $t/\tau_0 = 250$, the two central polarities, tightly connected by the dipped field lines beneath the surface, collide against each other, forming a closely-packed (δ -like) sunspot with a clearly defined PIL. The field lines show two expanded magnetic domes in the corona. The final surface flux is about four times the original axial values (Figure 8), which indicates that the flux tube comes in and out of the surface twice. The above pro-

cess is in good agreement with previous simulations (Toriumi et al. 2014; Fang & Fan 2015). Probably this AR can be categorized as $\beta\delta$ or $\beta\gamma\delta$.

The two flux tubes of the Inter-AR case follow a similar development process (Figure 7). However, since the two inner polarities are not connected by the subsurface field lines, they have almost no contact with each other and simply show a fly-by motion. Consequently, a strong field-gradient PIL is not created in this case. The final value of the surface magnetic flux is about four times the initial axial flux (Figure 8), which is again a behavior similar to the Quadrupole case. The above evolution is consistent with Case 2 of Toriumi et al. (2014). Contrary to the previous cases, the two ARs in this simulation should be simply regarded as β -spots.

4. FORMATION OF δ -SPOTS AND SHEARED PILS

As discussed in Section 1, sheared magnetic structures are thought to be important for the production of strong flare events. In particular, the sheared PIL in a δ -shaped sunspot is one of the most preferable locations for flare production. In this section, we show the detailed formation processes of δ -spots with sheared PILs for the four simulation cases.

4.1. Spot-Spot

Figure 9 summarizes the detailed photospheric evolution of the Spot-Spot case. In this case, as the twisted flux tube emerges, a complex magnetic pattern is formed in the surface layer and eventually an elongated PIL, highlighted by the Y -axis, is created at the center between the sunspot pair, P1 and N1. One prominent feature here is the counter-streaming shear flow along the PIL (see \mathbf{V}_h vector), with its orientation following the expansion of the magnetic arcades in the atmosphere. As a result of the shear flow, the horizontal magnetic field becomes highly inclined to the PIL direction (see \mathbf{B}_h vector) and the shear angle becomes almost 90° (see panel (k)). Here, the shear angle is measured from the direction of the potential field (the direction perpendicular to the PIL) and thus 90° is parallel to the PIL. The length of the highly-sheared ($\sim 90^\circ$) part along the PIL is $L_{\text{PIL}}/H_0 \sim 60$.

For easy comparison of the PIL with other simulation cases and actual observations, we introduce the diameter of a Reference sunspot. In the Reference case in Section 2.2, the final photospheric magnetogram at $t/\tau_0 = 300$ shows a simple bipolar pair (Figure 3). We measure the area of this Reference spot (region with $|B_z|/B_0 \geq 0.5$) and define D_{spot} as the diameter of the circle with an area equivalent to the area of this spot. Then, we obtain $D_{\text{spot}} = 24.6$, which is used as a normalizing factor for

length scale in Figures 9(k) and (l). With this value, one can find that the length of the highly-sheared PIL of the Spot-Spot case is as large as $L_{\text{PIL}}/D_{\text{spot}} = 2.5$.

One may also notice that the developed PIL has a strong horizontal field (see panel (i)). Moreover, this PIL reveals an alternating pattern of positive and negative polarities (see panels (h) and (l)). These features are highly reminiscent of the ‘‘magnetic channel’’ structure, which is introduced by Zirin & Wang (1993) as one of the key characteristics of the flare-producing PIL (Kubo et al. 2007; Wang et al. 2008). From the comparison with numerical simulations, Kusano et al. (2012) and Bamba et al. (2013) suggested the possibility that small-scale flux emergence at the magnetic channel in NOAA AR 10930 triggers the series of large flare eruptions.

4.2. Spot-Satellite

In the Spot-Satellite case, the newly emerging field in close proximity to the main sunspot of the opposite polarity creates a compact sheared PIL within a δ -spot. Figure 10 shows that the small bipole P2-N2 appears immediately right of ($+x$ -side of) the main spot N1. The horizontal flow field and the relative motion (middle column and panel (j)) indicate that, as N1 proceeds to the right, P2 drifts along the lower edge of ($-y$ -side of) N1 and produces a sheared PIL. Reflecting the scale of the parasitic tube and thus of the satellite spot, the length of the highly-sheared part of the PIL at $t/\tau_0 = 250$ is only $L_{\text{PIL}}/H_0 \sim 5$ or about 20% of the typical spot diameter, D_{spot} . Furthermore, in this case, the horizontal field is stronger at the PIL (see panel (f)).

The newly emerging fields at the edge of preexisting sunspots have been reported to drive major flares occasionally. For example, Louis et al. (2014) found that emerging satellite spots ahead of the leading sunspot of NOAA AR 11515 produce a filament at the PIL, which eventually erupts at the onset of the M5.6-class flare that develops into a CME: compare especially their Figure 7 and Figure 10 of this paper. Similar behaviors have been reported by, e.g., Wang et al. (1991), Ishii et al. (1998), Schmieder et al. (1994), and Takasaki et al. (2004), while simulations have shown that CME eruptions can be triggered by newly emerged flux at the edges of ARs (e.g. Chen & Shibata 2000).

In this case, as the satellite polarities (P2 and N2) move away from the main spot (N1), the δ -configuration and sheared PIL eventually disappear (see $t/\tau_0 = 280$ in Figure 10). The δ -spots are only seen in the earliest phase of the satellite emergence.

4.3. Quadrupole

Advection by horizontal flows (middle column of Figure 11), the two inner sunspots of the Quadrupole case, N1 and P2, collide with each other at the center of the simulation domain. The distance between the two spots show a monotonic decrease (panel (j)) and eventually a strongly packed δ -spot is created. The highly-sheared PIL has a length of $L_{\text{PIL}}/H_0 \sim 15$, or $L_{\text{PIL}}/D_{\text{spot}} \sim 0.6$, with the strongest B_z gradient (see panel (l)). The horizontal field is best enhanced at the central PIL (panel (i)).

Sun et al. (2012) showed that the Quadrupole AR NOAA 11158, producing the first X-class event in Cycle 24, hosts a highly-sheared PIL between the two colliding sunspots (Schrijver et al. 2011; Liu et al. 2012; Toriumi et al. 2013). They pointed out that the PIL has a strong horizontal field, which is in good agreement with the PIL simulated here: compare Figure 5 of Sun et al. (2012) and Figure 11 of this paper.

4.4. Inter-AR

The final case, Inter-AR, does not show the clear formation of a sheared PIL nor a δ -spot (Figure 12). The two inner sunspots, N1 and P2, remain separated from each other and simply show a fly-by motion (see panel (j)). In the central region in the photosphere, the horizontal field exhibits a slight indication of a magnetic shear (panel (g): Y -axis). However, the shear angle and the B_z gradient are not significant (panels (k) and (l)).

As mentioned in Section 1, the X1.2-class flare from NOAA ARs 11944 and 11943 produced a very fast CME. Möstl et al. (2015) pointed out the importance of AR magnetic structures in controlling the eruption of the CME. Although this flare event was not from the sheared PIL, it produced a fast CME that channeled through the open magnetic flux created between the two closed field systems, ARs 11944 and 11943.

4.5. Factors That Contribute to the Development of Sheared PIL

Among the four simulation cases of flare-productive ARs, we found that the Quadrupole case produces the highly-sheared PIL with the largest B_z gradient in a well developed δ -spot. In order to investigate the evolution of the sheared PIL, we take the Quadrupole case as an example and plot the terms of the induction equation in Figure 13. Here we show the shear component of the photospheric horizontal field, B_Y/B_0 , i.e., the magnetic field along the Y -axis in Figure 11(g), and each term of

the induction equation,

$$\frac{\partial B_Y}{\partial t} = \underbrace{(\mathbf{B} \cdot \nabla) V_Y}_{\text{Stretching}} - \underbrace{(\mathbf{V} \cdot \nabla) B_Y}_{\text{Advection}} - \underbrace{\left(\frac{\partial V_X}{\partial X} + \frac{\partial V_Y}{\partial Y} \right) B_Y}_{\text{Compression (horizontal)}} - \underbrace{\frac{\partial V_z}{\partial z} B_Y}_{\text{Compression (vertical)}} \quad (19)$$

In Equation (19), we neglect the magnetic diffusion and divide the compression term, $-(\nabla \cdot \mathbf{V}) B_Y$, into the horizontal and vertical components.

It is seen from Figure 13 that the shear field B_Y/B_0 appears at $t/\tau_0 = 230$, peaks around $t/\tau_0 = 275$, and then gradually decays. During this period, the advection term is initially dominant ($t/\tau_0 \lesssim 260$) and, as the advection weakens, the stretching term increases and becomes comparable to the advection term ($260 \lesssim t/\tau_0 \lesssim 280$). For most of the time, the two compression terms remain negative and do not contribute to the growth of the shear. In the final phase after B_Y attains its peak ($t/\tau_0 \gtrsim 280$), the total value becomes negative and thus B_Y decreases. However, the horizontal compression turns positive and becomes the only term that works to sustain B_Y .

The above behavior can be explained in the following manner. In the Quadrupole case, the sunspots of positive and negative polarities (N1 and P2 in Figure 11) approach to the region center and produce a δ -like configuration. In the early phase, as the two spots come closer, they transport the horizontal field from both sides (see the horizontal field vector shown with red arrows in Figure 11). This effect enhances the advection term in the early phase (Figure 13). Then, after the two spots merge, they show a drifting motion (N1 to the right and P2 to the left: yellow arrows in Figure 11), which stretches the horizontal field along the PIL, leading to the enhancement of the stretching term in the later phase (Figure 13). The compression by the two approaching spots also becomes stronger. However, this is only true for the horizontal component (Figure 13). Since the emergence is a process of a nonlinear instability, the rising field drastically expands vertically and $\partial V_z/\partial z$ is positive (e.g., Shibata et al. 1989). The negative contribution of the vertical compression term in Figure 13 reflects this process.

5. MAGNETIC STRUCTURES AND ENERGY BUILDUP IN THE ATMOSPHERE

5.1. Magnetic Structures

Figure 14 summarizes the 3D magnetic field structures for the four simulation cases. For the Spot-Spot case, the green magnetic field lines, each connecting the

main spot and the extended tail, approach the center of the domain from both sides and form an electric current sheet between them (indicated by an isosurface in the middle column: see Appendix A for the plotted values). As a result, the green field lines reconnect with each other and create the purple and yellow field lines. The newly created purple flux system is highly sheared and aligned almost parallel to the photospheric PIL. However, this purple flux is trapped by the overlying yellow flux that connects the two main sunspots.

In the Spot-Satellite case, as the main flux tube (yellow) pushes up the parasitic tube (green), magnetic reconnection occurs between the two flux tubes and the purple field lines are formed. One may find that, in the subsurface layer, the purple field lines extend to both the main and parasitic flux tubes. The current sheet is developed between the two flux systems immediately above the sheared PIL in the photosphere. Reflecting the smaller scale of the PIL (Figure 10), the purple flux is compact and very low-lying compared to the other cases. Contrary to Spot-Spot, this purple flux is located at the edge of the AR, and is not trapped by the overlying fields, i.e., exposed to the outer space.

The Quadrupole and Inter-AR cases somewhat resemble each other. As explained in Section 3, the two emerging flux systems of the Quadrupole case (yellow and green) originate from the common single flux tube and thus are connected beneath the surface. Consequently, the two photospheric polarities show convergence motion and become tightly packed. Driven by this photospheric motion, magnetic reconnection between the two coronal loops occurs in the current layer with a sheet-like shape extending in parallel with the photospheric PIL. Eventually, the purple flux system is newly created, which short-circuits the two inner polarities.

Although the two coronal loops of the Inter-AR case are not originally connected beneath the surface and, consequently, the contact of the two flux systems is less vigorous, they in fact undergo magnetic reconnection in the atmosphere since the two bipoles expand above the surface. A vertically extending current sheet is seen in between. The two bipoles eventually form purple field lines that connect the two independent ARs, which may be related to the flux rope that erupted as a fast CME between NOAA 11944 and 11943 (Möstl et al. 2015).

5.2. Buildup of Magnetic Energy

In order to examine the accumulation of magnetic energy in the atmosphere, we calculate the potential magnetic fields from the B_z map at $z_p/H_0 = 2$ and measure

the total magnetic energy

$$E_{\text{mag}} = \int_{z \geq z_p} \frac{B^2}{8\pi} dV, \quad (20)$$

potential energy

$$E_{\text{pot}} = \int_{z \geq z_p} \frac{B_{\text{pot}}^2}{8\pi} dV, \quad (21)$$

and free energy

$$\Delta E_{\text{mag}} \equiv E_{\text{mag}} - E_{\text{pot}}. \quad (22)$$

Figure 15 compares the time evolutions of E_{mag} , E_{pot} , and ΔE_{mag} for the four cases. The time $\Delta t/\tau_0$ is measured since the flux appears at the photosphere. Here, the simulation case with the largest energy is the Spot-Spot case. Reflecting the large photospheric flux (Figure 8), it has a total energy and free energy that are about one order of magnitude greater than those of the other three cases.

The free energy of the Spot-Satellite case is larger than that of the Reference case because free energy is stored in the current layer between the main and parasitic tubes in the Spot-Satellite case (see Figure 14, Spot-Satellite). Since the current sheet lies lower in the atmosphere, where the density is higher and the reconnection is less effective (Section 2.1), the free energy is not significantly consumed and gradually increases over time.

The free energies of the remaining two cases exhibit an interesting oscillatory behavior. For example, Quadrupole shows a big bump around $\Delta t/\tau_0 = 50$, which corresponds to $t/\tau_0 = 270$. This is because, whereas the potential energy (E_{pot}) follows the monotonous growth of the photospheric flux (Figure 8), coronal reconnection between the two magnetic loops occurs when the two inner polarities approach from $t/\tau_0 = 240$ (Figure 6) and the actual magnetic energy (E_{mag}) starts reduction, leading to the drastic loss of the free energy. The free energy decrease of Inter-AR after $\Delta t/\tau_0 = 40$ (corresponding to $t/\tau_0 = 260$) is also due to the coronal reconnection of the two magnetic systems, which occurs later than in the Quadrupole case because the two systems are significantly separated from each other.

The bottom panel of Figure 15 is intended to compare the four cases under the condition that they have similar AR scales. For each simulation case, we normalize the free energy by the three-halves power of its total unsigned flux at the final stage ($t/\tau_0 = 300$), $\Phi_{\text{final}}^{3/2}$. Note that the AR area is approximately proportional to the total unsigned flux, Φ , because the photospheric field

is almost uniquely determined by the pressure balance between the magnetic field and the external gas. Considering that the AR volume is roughly proportional to the area to the 3/2, here we normalize the free magnetic energies of the four different cases with $\Phi^{3/2}$.

One can find that, since the difference among the four cases in the bottom panel is less prominent than that in the middle panel, the free energy depends highly on the photospheric total flux of each AR (or equivalently area or volume). However, as seen from the bottom panel, even for ARs of the similar size scales, the stored free energy may differ much, up to a factor of five, depending on the twist and geometrical configuration of subsurface emerging fields.

6. FLARE AND CME PREDICTIONS BASED ON PHOTOSPHERIC MEASUREMENTS

6.1. Flare Predictions

The prediction of flares and CMEs is currently one of the most important topics of solar-terrestrial physics. Since the measurement of the photospheric parameters from vector magnetic data is much easier than the reconstruction of full 3D magnetic fields, most of the current flare prediction schemes are based on such photospheric parameters. After [Leka & Barnes \(2003\)](#) and [Barnes et al. \(2007\)](#) made use of the vector magnetogram for flare prediction, [Bobra & Couvidat \(2015\)](#) extracted various parameters (including those suggested by [Leka & Barnes 2003](#), [Schrijver 2007](#), and [Fisher et al. 2012](#)) from the *SDO*/HMI vector magnetogram for each AR (SHARP data: [Bobra et al. 2014](#)) and obtained good predictive performance for flares of \geq M1.0-class using a machine learning algorithm. By adding flare history and ultraviolet observables to the SHARP parameters, [Nishizuka et al. \(2017\)](#) further developed flare prediction models with even higher performance (see also [Muranushi et al. 2015](#); [Liu et al. 2017](#)). The SHARP parameters used by these authors are summarized in [Table 1](#). The F -score (Fisher score) in the table indicates the scoring of the parameter given by [Bobra & Couvidat \(2015\)](#).

Then, the question is as follows. Why do some of these parameters predict the flare eruptions well (indicated by larger F -scores), while the others do not (smaller F)? The series of numerical simulations of the present work, which successfully reproduced a variety of complex, non-potential configurations of flare-productive ARs, is one of the best ways to resolve this mystery. It is worth noting that [Guennou et al. \(2017\)](#) recently examined various photospheric parameters using simulations proposed by [Leake et al. \(2013, 2014\)](#) and found that parameters related to the PIL are the best to describe the flare oc-

currence. However, their analysis was restricted by the limited size of ARs and complexity of the simulations, which could be compensated for by our simulations.

Considering that the flare occurrence is a releasing process of free magnetic energy stored in the atmosphere, we compare the SHARP parameters in [Table 1](#) and the stored free energy, i.e., the maximum flare energy that could potentially be released, for the four simulation cases. The top six panels of [Figure 16](#) show samples of the comparisons. In each diagram, the horizontal axis represents a SHARP parameter in question that is measured at the surface ($z_p/H_0 = 2$) every $\Delta t/\tau_0 = 2$ after the flux appears at the surface, whereas the vertical axis represents the stored free magnetic energy at each moment ($\Delta E_{\text{mag}}/E_0$, measured directly from the 3D computational domain: see [Section 5.2](#)). One can find that some SHARP parameters have strong proportionalities with the free energy (e.g., TOTUSJH and TOTPOD), while others do not (e.g., EPSY and EPSX). It is reasonable that parameters such as TOTUSJH (total unsigned current helicity) show high correlations because the free energy is stored in the form of electric current.

For each diagram, we compute the correlation coefficient, CC , in a log-log plot, which indicates how accurately a given SHARP parameter reflects the stored free energy, and show it in the bottom right of the diagram. For each plot, we assume each data point to be independent and simply derive CC from all data points, regardless of the simulation cases. Therefore, there is only one CC for each plot. The CC values for all 25 parameters are summarized in [Table 1](#).

The bottom panel of [Figure 16](#) is a scatter plot of absolute correlation, $|CC|$, vs. F -score for all SHARP parameters. It is clearly seen that parameters with larger F yield larger $|CC|$. In other words, the SHARP parameters that are excellent in predicting the flare events can predict the free energy in the atmosphere very accurately. On the other hand, the smaller- F parameters have weaker to almost no correlation with the free energy, indicating that they are incapable of predicting the free energy. It should be noted that, in each scatter plot, the correlation is strong (weak) because all four simulations show consistently strong (weak) correlations. For example, $|CC|$ of TOTPOT is 0.95, which is due to high correlations of the four cases: 0.89 (Spot-spot), 0.85 (Spot-satellite), 0.82 (Quadrupole), and 0.98 (Inter-AR).

The above relationship between $|CC|$ and F confirms the suggestion by [Welsch et al. \(2009\)](#) that parameters strongly associated with the flare activity are extensive (scaling with AR size: indicated by ‘‘E’’ in [Table 1](#))

because the free energy is likely stored on large scales and non-local.

The even higher prediction rates obtained by Nishizuka et al. (2017) are probably because, besides adding flare history, they include ultraviolet observables that are sensitive to chromospheric dynamics such as triggering processes (preflare brightenings) before the flares occur (see, e.g., Bamba et al. 2013 for detailed observational analysis of the flare triggers). This suggests that, although the SHARP parameters properly indicate the accumulation of free energy, this is not sufficient to accurately predict the exact occurrence of flares, and we need additional observables that represent the triggering of the flares.

6.2. CME Predictions

The rightmost column of Table 1 shows the ranking of SHARP parameters for predicting CME eruptions, as reported by Bobra & Ionidis (2016). Contrary to the flare prediction case, the parameters that successfully predict whether a given flare produces a CME are mostly intensive (independent of AR size: indicated by ‘‘I’’ in Table 1), not extensive. One can also see from this table that they show moderate to weak negative correlations ($CC < 0$) between the SHARP parameters and the stored free energy. This is because these parameters are, in most cases, normalized by the AR size or some relevant factors. That is, the CME-predictive parameters are not perfectly independent of the AR size; rather, they have negative dependence with the AR scale.

For example, according to Bobra & Ionidis (2016), MEANGBT is one of the highest-ranking CME parameters, and it is the sum of the horizontal magnetic gradient normalized by the SHARP patch pixels N (representing AR area):

$$|\nabla B_{\text{tot}}| = \frac{\sum \sqrt{\left(\frac{\partial B}{\partial x}\right)^2 + \left(\frac{\partial B}{\partial y}\right)^2}}{N}. \quad (23)$$

Since the flare-causing PILs tend to have a high magnetic gradient (Section 1), the numerator of Equation (23) becomes larger for flaring ARs. However, the normalization by area cancels this trend, leading to a negative correlation with the free energy ($CC = -0.530$; Figure 16) and thus a worse flare prediction rate ($F = 192.3$). Still, this parameter yields a high CME prediction performance. This may also be due to the normalization effect. That is, while the local flaring zone is characterized by the field gradient (numerator), the global scale of the AR is represented by the AR area (denominator), and the relationship between the two factors (their ratio) determines the CME productivity.

The above discussion is further supported by observational studies. Sun et al. (2015) investigated the flare-rich but CME-poor AR NOAA 12192 and found that this AR has a relatively weak non-potentiality with a relatively strong overlying field and, thus, the flux ropes fail to erupt as CMEs. They concluded that CME eruption is described by the relative measure of non-potentiality over the restriction of the background field. A statistical analysis by Toriumi et al. (2017) revealed that CME-less ARs show, on average, smaller $S_{\text{ribbon}}/S_{\text{spot}}$ (flare ribbon area normalized by total sunspot area) and $|\Phi|_{\text{ribbon}}/|\Phi|_{\text{AR}}$ (total unsigned magnetic flux in the ribbon normalized by the total unsigned flux of the entire AR). They argued that the magnetic relation between the large-scale structure of an AR and the localized flaring domain within it is a key factor determining the CME eruption. We shall leave the detailed numerical investigation on the relation for future work.

7. SUMMARY

In this paper, aiming at understanding the creation of flare-productive ARs, especially the formation processes of δ -spots and sheared PILs and the accumulation of free magnetic energy, we performed flux emergence simulations of four typical types of flaring ARs (Zirin & Liggett 1987; Toriumi et al. 2017). The four simulations share similar numerical conditions (tube’s initial axial field, background atmosphere, etc.) in order that one can easily compare the results. The main results of this study are summarized as follows.

The first category of the four types of ARs, Spot-Spot, is modeled by an emergence of a tightly-twisted, kink-unstable flux tube from the convection zone (Fan et al. 1999; Takasao et al. 2015). Because of the kink instability, the tube’s ascent is fastest among the four cases. The flux tube eventually produces a complex AR composed of two main sunspots of both polarities with extended tails, which is probably classified as $\beta\gamma\delta$. As the main spots develop, an elongated sheared PIL spanning over the entire AR is created at the center, which shows a stripe pattern of both polarities that is highly reminiscent of the magnetic channel (Zirin & Wang 1993). Owing to magnetic reconnection of the two loop systems, sheared arcade fields are newly formed above the central PIL. Although this configuration has no clear access to the outer atmosphere, the quadrupolar structure achieved here (main spots and extended tails) is preferable for CME (e.g. Antiochos et al. 1999; Hirose et al. 2001). This AR possesses the largest unsigned flux in the photosphere with the largest free energy in the corona. That is, even if we use the flux tubes with the same axial flux, the photospheric unsigned flux can differ by up to

one order of magnitude depending on the initial twist and geometry.

The Spot-Satellite AR is achieved by the interaction of main and parasitic flux tubes. As the parasitic tube appears at the photosphere in the close vicinity of the main spot, they form tiny δ -spots at the edge of the AR with a compact sheared PIL ($\beta\gamma\delta$ spot). The newly formed field lines, created through magnetic reconnection between the two flux tubes, are clearly exposed to the upper atmosphere.

The Quadrupole AR is modeled by the emergence of a single flux tube that rises at two buoyant sections (Toriumi et al. 2014; Fang & Fan 2015). The two emerging bipoles collide against each other at the center and create a strongly packed δ -spot and a sheared PIL with the highest B_z gradient (classified as $\beta\gamma$ or $\beta\gamma\delta$). The coronal free energy shows a fluctuation with time, coincident with the magnetic reconnection of the two emerging bipoles.

The two flux tubes of the Inter-AR case, placed in the convection zone in a parallel fashion, totally separated from each other, produce two independent ARs on the solar surface. The two tubes, however, undergo magnetic reconnection in the corona as they expand in the atmosphere, and consequently, a new flux system connecting the two ARs is formed. Although they have no clear sheared PIL nor a δ -spot and thus should be classified as two simple β -spots, they in fact can produce X-class flares if the free energy is sufficiently accumulated, which could launch a fast CME (Möstl et al. 2015; Wang et al. 2015)².

The sheared PIL in a δ -spot is formed by the combination of different factors (Figure 13). The enhancement of the sheared field is at first due to the advection. As the spots of opposite polarities come closer to each other, they transport the horizontal flux to the PIL in between. Then, the (relative) drifting motion of the two spots stretches the horizontal flux, and thus, the shear component grows further. The horizontal compression, which is the pressing motion caused by the two approaching spots, also contributes to the intensification of the horizontal flux.

Some of the SHARP parameters, the photospheric observables obtained from vector magnetograms, are known to predict the solar flares with high accuracy (Bobra & Couvidat 2015). From the δ -spot models of

this paper, we confirmed that these parameters reflect the free magnetic energy stored in the corona very well. Since the free energy is a global (non-local) value, the extensive parameters, i.e., those scaling with the AR size, show higher prediction scores (Welsch et al. 2009). For even better flare forecast, we may need to add parameters that are sensitive to the triggering of the flares, such as chromospheric brightenings (Nishizuka et al. 2017; Muranushi et al. 2015).

On the other hand, it was also found that most of the CME-predictive SHARP parameters (Bobra & Ilonidis 2016) do not reflect the coronal free energy well: they show moderate to lower correlation with the free energy. These parameters are the values normalized by the AR size or some relevant factors. This indicates the importance of the magnetic relation between local flaring zones (e.g. erupting flux rope) and large-scale circumstances (e.g. overlying arcades) for CME productivity (Sun et al. 2015; Toriumi et al. 2017).

8. DISCUSSION

From the numerical simulations, we derived the close connections among the subsurface history of emerging flux, the free magnetic energy stored in the atmosphere, and the various SHARP parameters measured at the surface. For example, the flare-predictive parameters are strongly correlated with the free energy (Figure 16), while the free energy highly depends on the types of the emerging flux (Figure 15). These relationships obtained in this work provide important information such as which parameters are suitable, not only for predicting flares and CMEs, but also for probing the subsurface state of emerging flux that builds up flare-productive ARs.

Although we revealed the detailed formation of δ -spots and sheared magnetic structures, how the complexity of subsurface emerging flux is produced remained unclear. Recently, Jaeggli & Norton (2016) found that, whereas the fractions of all α - and β -sunspots remain constant over solar cycles (roughly 20% and 80%, respectively), the fraction of complex ARs, appended with γ and/or δ , increases drastically from less than 10% at solar minimum to more than 30% at maximum. From this result, they suggested the possibility that complex ARs are produced by the collision of simple ARs around the surface layer due to the higher frequency of flux emergence during solar maximum.

This situation is more in favor of the Spot-Satellite model, in which two flux systems interact with each other in the subsurface region (Fan et al. 1998). Such interaction may be a stochastic process, probably coupled with convective dynamics. Therefore, we need global dy-

² Like other simulation cases, the CME-predictive SHARP parameters of the Inter-AR case show inversely correlated trends with the free energy (see e.g. MEANGBT of Figure 16), which supports the possibility of CME eruptions from the Inter-AR configuration.

namo simulations to investigate how the emerging fluxes interact with each other and with convection cells (e.g. Nelson et al. 2014).

Another remaining problem is that we did not observe any flare eruptions in the simulations. To follow the full story from the emergence to eruption including free energy accumulation, current sheet formation, and reconnection onset (Manchester et al. 2004; Archontis et al. 2014; Leake et al. 2014), we may need to improve the model, for example, by tracing an even longer evolution in a wider simulation domain (see Oi 2017 for emergence-to-eruption simulation of the Quadrupole case). Photospheric and subsurface convection may

supply magnetic shear and affect long-term evolution of magnetic configuration, which should be investigated further in future (Fang et al. 2012; Chatterjee et al. 2016).

The authors are grateful to the anonymous referee for improving the manuscript. S.T. and S.T. would like to thank M.C.M. Cheung for providing the potential field calculation code. This work was supported by JSPS KAKENHI Grant Numbers JP16K17671, JP15H05814, JP16J02063. Numerical computations were carried out on Cray XC30 at Center for Computational Astrophysics, National Astronomical Observatory of Japan.

APPENDIX

A. VISUALIZATION OF CURRENT SHEETS

From Equation (7), we can roughly estimate the thickness of the current sheet, δ :

$$J \sim \frac{1}{4\pi} |\nabla \times \mathbf{B}| \sim \frac{1}{4\pi} \frac{B}{\delta}, \quad (\text{A1})$$

or

$$\delta \sim \frac{1}{4\pi} \frac{B}{J}. \quad (\text{A2})$$

In the numerical simulations, the magnetic field lines start reconnection when the current thickness becomes comparable to the grid spacing. If we express the typical grid size as $\Delta = \min(\Delta x, \Delta y, \Delta z)$, the non-dimensional parameter

$$\hat{J} = \frac{\Delta}{\delta} = \frac{4\pi J}{B} \Delta \quad (\text{A3})$$

approaches unity in the core of the current layer. In Figure 14, we show the region of $\hat{J} \geq 8 \times 10^{-3}$ with isocontours (sky blue) instead of simply plotting J .

REFERENCES

- Antiochos, S. K., DeVore, C. R., & Klimchuk, J. A. 1999, *ApJ*, 510, 485
- Archontis, V., Hood, A. W., & Tsinganos, K. 2014, *ApJL*, 786, L21
- Archontis, V., Moreno-Insertis, F., Galsgaard, K., Hood, A., & O’Shea, E. 2004, *A&A*, 426, 1047
- Bamba, Y., Kusano, K., Yamamoto, T. T., & Okamoto, T. J. 2013, *ApJ*, 778, 48
- Barnes, G., Leka, K. D., Schumer, E. A., & Della-Rose, D. J. 2007, *Space Weather*, 5, 9002
- Bobra, M. G., Sun, X., Hoeksema, J. T., et al. 2014, *SoPh*, 289, 3549
- Bobra, M. G., & Couvidat, S. 2015, *ApJ*, 798, 135
- Bobra, M. G., & Ilonidis, S. 2016, *ApJ*, 821, 127
- Chatterjee, P., Hansteen, V., & Carlsson, M. 2016, *Physical Review Letters*, 116, 101101
- Chen, P. F., & Shibata, K. 2000, *ApJ*, 545, 524
- Cheung, M. C. M., & Isobe, H. 2014, *Living Reviews in Solar Physics*, 11, 3
- Cheung, M. C. M., Rempel, M., Title, A. M., & Schüssler, M. 2010, *ApJ*, 720, 233
- Dedner, A., Kemm, F., Kröner, D. et al. 2002, *Journal of Computational Physics*, 175, 645
- Falconer, D. A., Moore, R. L., & Gary, G. A. 2002, *ApJ*, 569, 1016
- Fan, Y. 2001, *ApJL*, 554, L111
- Fan, Y., Zweibel, E. G., & Lantz, S. R. 1998, *ApJ*, 493, 480
- Fan, Y., Zweibel, E. G., Linton, M. G., & Fisher, G. H. 1999, *ApJ*, 521, 460

- Fang, F., & Fan, Y. 2015, *ApJ*, 806, 79
- Fang, F., Manchester, IV, W., Abbett, W. P., & van der Holst, B. 2012, *ApJ*, 754, 15
- Fisher, G. H., Bercik, D. J., Welsch, B. T., & Hudson, H. S. 2012, *SoPh*, 277, 59
- Guo, J., Lin, J., & Deng, Y. 2014, *MNRAS*, 441, 2208
- Guennou, C., Pariat, E., Vilmer, N., & Leake, J. E. 2017, *Journal of Space Weather and Space Climate*, 7, A17
- Hagyard, M. J., Teuber, D., West, E. A., & Smith, J. B. 1984, *SoPh*, 91, 115
- Hirose, S., Uchida, Y., Uemura, S., Yamaguchi, T., & Cable, S. B. 2001, 551, 586
- Ishii, T. T., Kurokawa, H., & Takeuchi, T. T. 1998, *ApJ*, 499, 898
- Jaeggli, S. A., & Norton, A. A. 2016, *ApJL*, 820, L11
- Kleint, L., Battaglia, M., Reardon, K. et al. 2015, *ApJ*, 806, 9
- Kubo, M., Yokoyama, T., Katsukawa, Y., et al. 2007, *PASJ*, 59, S779
- Künzel, H. 1960, *Astronomische Nachrichten*, 285, 271
- Kurokawa, H. 1987, *SoPh*, 113, 259
- Kusano, K., Bamba, Y., Yamamoto, T. T., et al. 2012, *ApJ*, 760, 31
- Leake, J. E., Linton, M. G., & Antiochos, S. K. 2014, *ApJ*, 787, 46
- Leake, J. E., Linton, M. G., & Török, T. 2013, *ApJ*, 778, 99
- Leka, K. D., & Barnes, G. 2003, *ApJ*, 595, 1296
- Linton, M. G., Longcope, D. W., & Fisher, G. H. 1996, *ApJ*, 469, 954
- Liu, C., Deng, N., Liu, R., et al. 2012, *ApJL*, 745, L4
- Liu, C., Deng, N., Wang, J. T. L., & Wang, H. 2017, *ApJ*, 843, 104
- López Fuentes, M. C., Demoulin, P., Mandrini, C. H., & van Driel-Gesztelyi, L. 2000, *ApJ*, 544, 540
- López Fuentes, M. C., Démoulin, P., Mandrini, C. H., Pevtsov, A. A., & van Driel-Gesztelyi, L. 2003, *A&A*, 397, 305
- Louis, R. E., Puschmann, K. G., Kliem, B., Balthasar, H., & Denker, C. 2014, *A&A*, 562, A110
- Manchester, IV, W., Gombosi, T., DeZeeuw, D., & Fan, Y. 2004, *ApJ*, 610, 588
- Möstl, C., Rollett, T., Frahm, R. A., et al. 2015, *Nature Communications*, 6, 7135
- Muranushi, T., Shibayama, T., Muranushi, et al. 2015, *Space Weather*, 13, 778
- Murray, M. J., Hood, A. W., Moreno-Insertis, F., Galsgaard, K., & Archontis, V. 2006, *A&A*, 460, 909
- Nelson, N. J., Brown, B. P., Sacha Brun, A., Miesch, M. S., & Toomre, J. 2014, *SoPh*, 289, 441
- Nishizuka, N., Sugiura, K., Kubo, Y., et al. 2017, *ApJ*, 835, 156
- Oi, Y. 2017, Master thesis, Univ. Tokyo
<http://www-space.eps.s.u-tokyo.ac.jp/group/yokoyama-lab/theses>
- Parker, E. N. 1955, *ApJ*, 121, 491
- Priest, E. R., & Forbes, T. G. 2002, *A&A Rv*, 10, 313
- Rempel, M., & Cheung, M. C. M. 2014, *ApJ*, 785, 90
- Rempel, M., Schüssler, M., & Knölker, M. 2009, *ApJ*, 691, 640
- Sammis, I., Tang, F., & Zirin, H. 2000, *ApJ*, 540, 583
- Schmieder, B., Hagyard, M. J., Guoxiang, A., et al. 1994, *SoPh*, 150, 199
- Schrijver, C. J. 2007, *ApJL*, 655, L117
- Schrijver, C. J., Aulanier, G., Title, A. M., Pariat, E., & Delannée, C. 2011, *ApJ*, 738, 167
- Shi, Z., & Wang, J. 1994, *SoPh*, 149, 105
- Shibata, K., & Magara, T. 2011, *Living Reviews in Solar Physics*, 8, 6
- Shibata, K., Tajima, T., Steinolfson, R. S., & Matsumoto, R. 1989, *ApJ*, 345, 584
- Sun, X., Bobra, M. G., Hoeksema, J. T., et al. 2015, *ApJL*, 804, L28
- Sun, X., Hoeksema, J. T., Liu, Y., et al. 2012, *ApJ*, 748, 77
- Takasaki, H., Asai, A., Kiyohara, J., et al. 2004, *ApJ*, 613, 592
- Takasao, S., Fan, Y., Cheung, M. C. M., & Shibata, K. 2015, *ApJ*, 813, 112
- Takizawa, K., & Kitai, R. 2015, *SoPh*, 290, 2093
- Tanaka, K. 1991, *SoPh*, 136, 133
- Toriumi, S., Iida, Y., Bamba, Y., et al. 2013, *ApJ*, 773, 128
- Toriumi, S., Iida, Y., Kusano, K., Bamba, Y., & Imada, S. 2014, *SoPh*, 289, 3351
- Toriumi, S., Schrijver, C. J., Harra, L. K., Hudson, H., & Nagashima, K. 2017, *ApJ*, 834, 56
- Toriumi, S., & Yokoyama, T. 2011, *ApJ*, 735, 126
- Toriumi, S., & Yokoyama, T. 2012, *A&A*, 539, A22
- Vögler, A., Shelyag, S., Schüssler, M., et al. 2005, *A&A*, 429, 335
- Wang, H., Jing, J., Tan, C., Wiegmann, T., & Kubo, M. 2008, *ApJ*, 687, 658
- Wang, H., & Liu, C. 2015, *Research in Astronomy and Astrophysics*, 15, 145
- Wang, H., Tang, F., Zirin, H., & Ai, G. 1991, *ApJ*, 380, 282
- Wang, R., Liu, Y. D., Dai, X., et al. 2015, *ApJ*, 814, 80
- Welsch, B. T., Li, Y., Schuck, P. W., & Fisher, G. H. 2009, *ApJ*, 705, 821
- Zirin, H., & Liggett, M. A. 1987, *SoPh*, 113, 267
- Zirin, H., & Wang, H. 1993, *Nature*, 363, 426

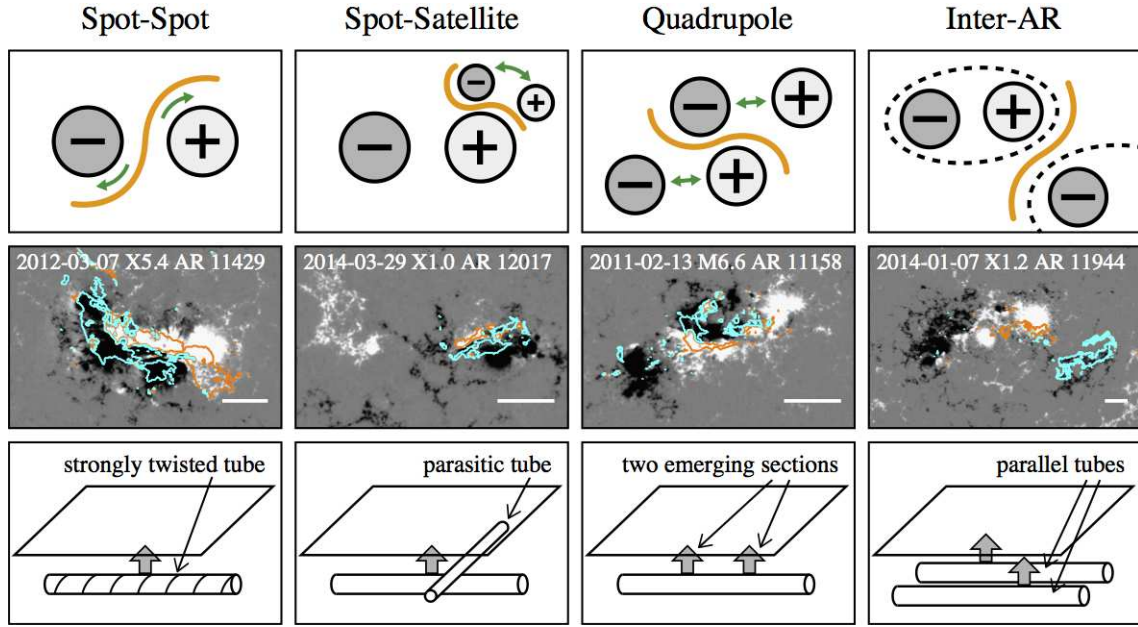


Figure 1. Four categorizations of flaring ARs. Top row: polarity distributions, in which sunspots are indicated by circles with plus and minus signs. Sheared PIL involved in flare eruptions is shown with an orange line, whereas the proper spot motions are indicated with green arrows. Second row: sample flare events. *SDO*/HMI magnetogram is shown as background and the orange and turquoise contours indicate the flare ribbons detected by AIA 1600 Å in the positive and negative polarities, respectively. Date, *GOES* flare class, and NOAA AR number are presented. White bar indicates a length of 50'' (~ 36.3 Mm). Bottom row: schematic diagrams showing the numerical setup of the four simulation cases (Section 2.3). Top and second rows reproduced from Toriumi et al. (2017).

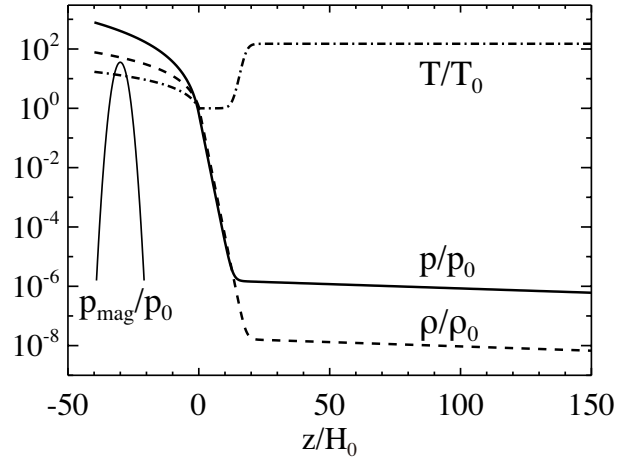


Figure 2. One-dimensional (z -)distributions of the initial background density (thick solid), pressure (dashed), and temperature (dash-dotted). The magnetic pressure $p_{\text{mag}} = B^2/(8\pi)$ along the vertical axis $x = y = 0$ of the Reference case is overlotted (thin solid).

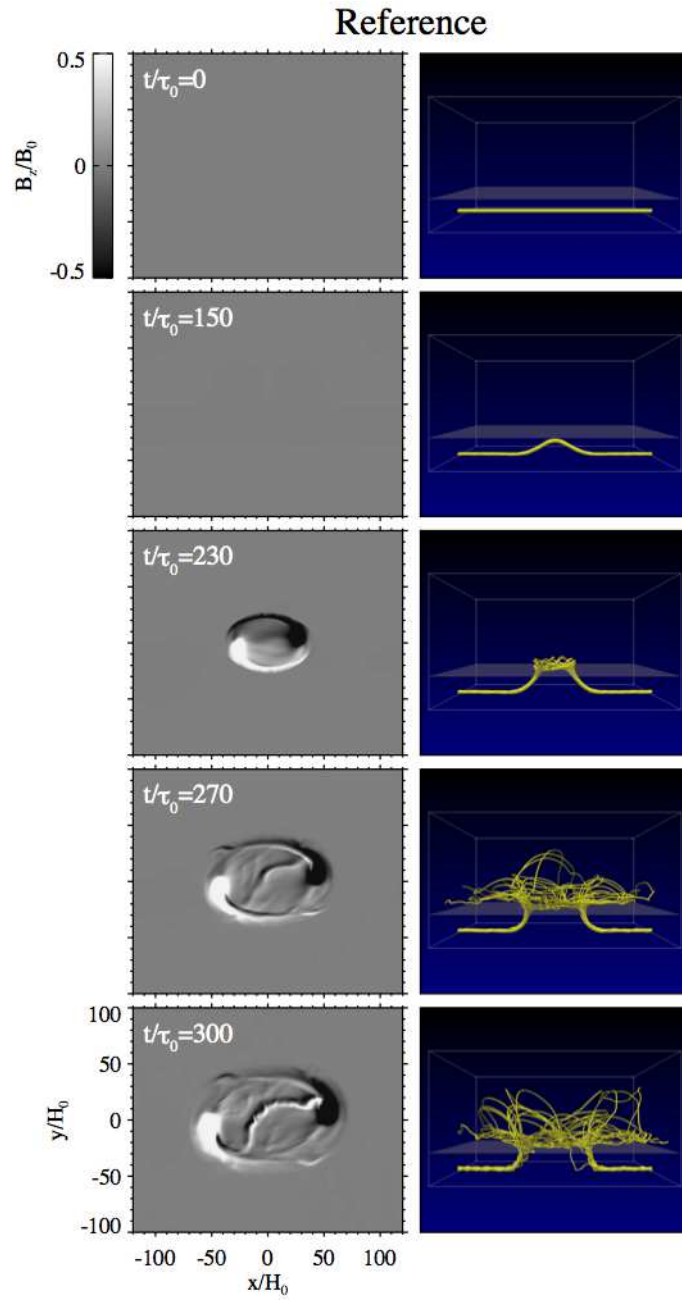


Figure 3. Evolution of surface vertical magnetic fields and magnetic field lines for the Reference case. See the accompanying video for the temporal evolution.

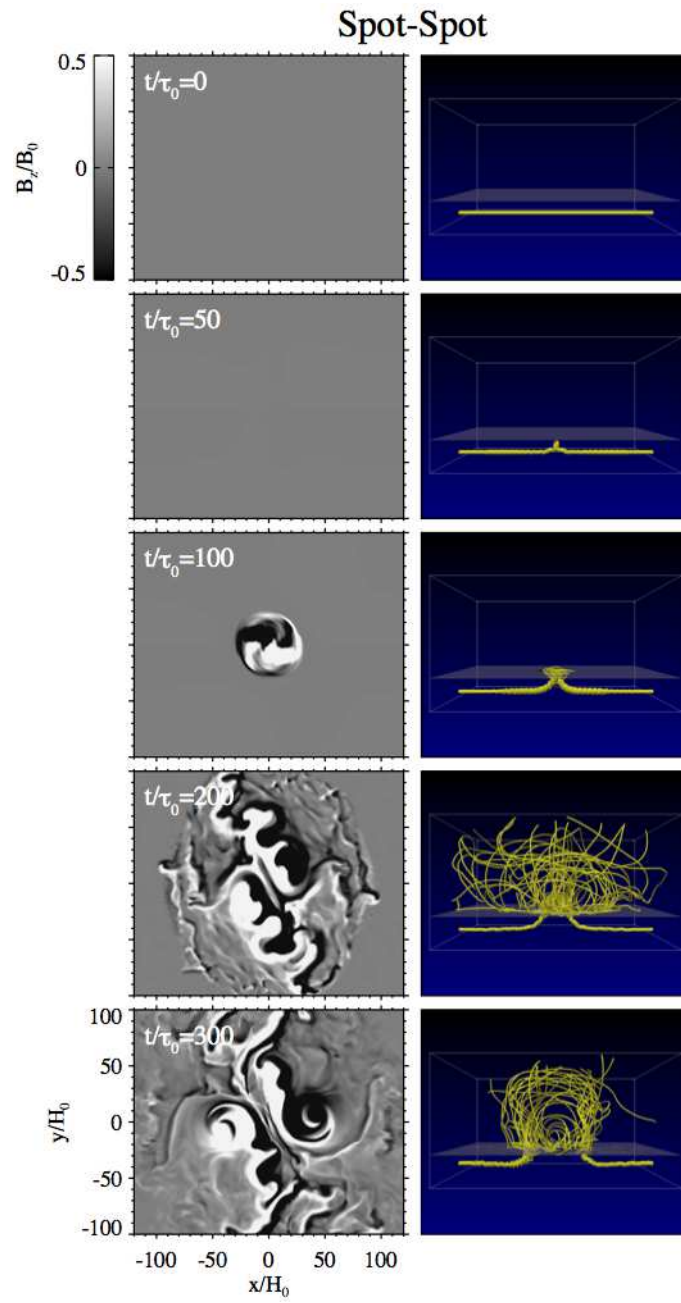


Figure 4. Same as Figure 3 but for the Spot-Spot case.

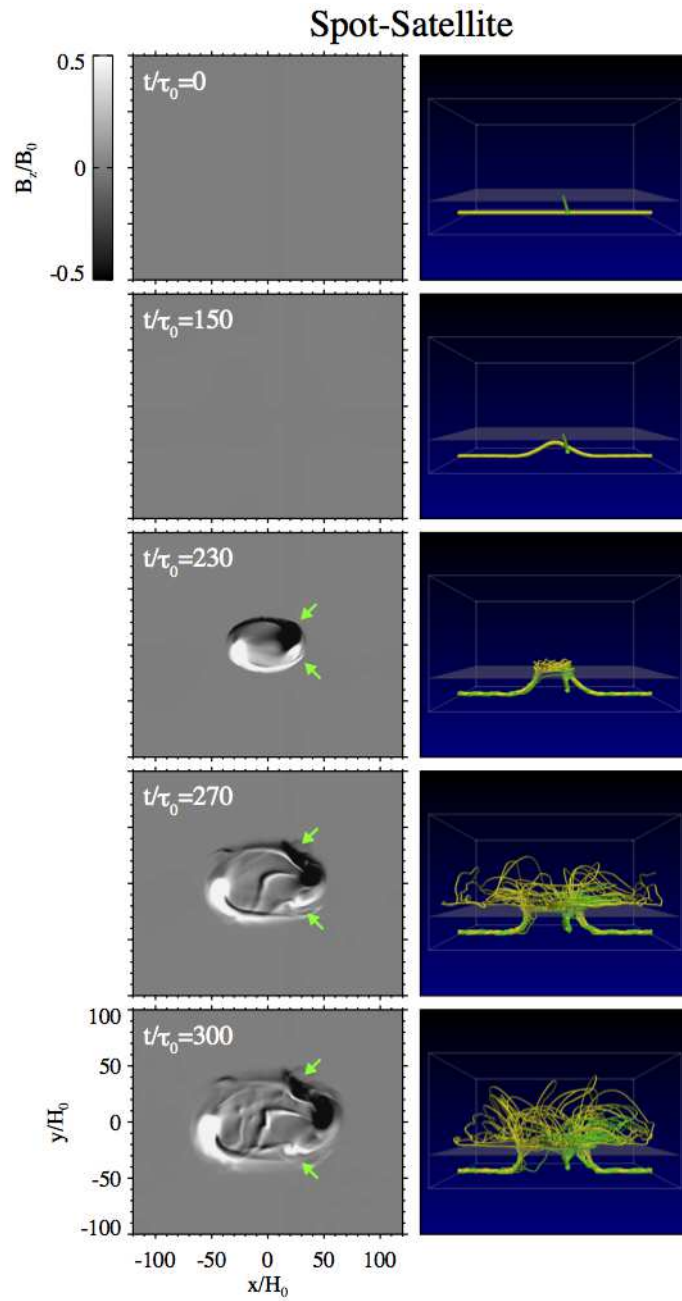


Figure 5. Same as Figure 3 but for the Spot-Satellite case. The green arrows in the magnetograms indicate the satellite spots, which originate from the parasitic flux tube, while the green field lines in the right column are for the parasitic tube.

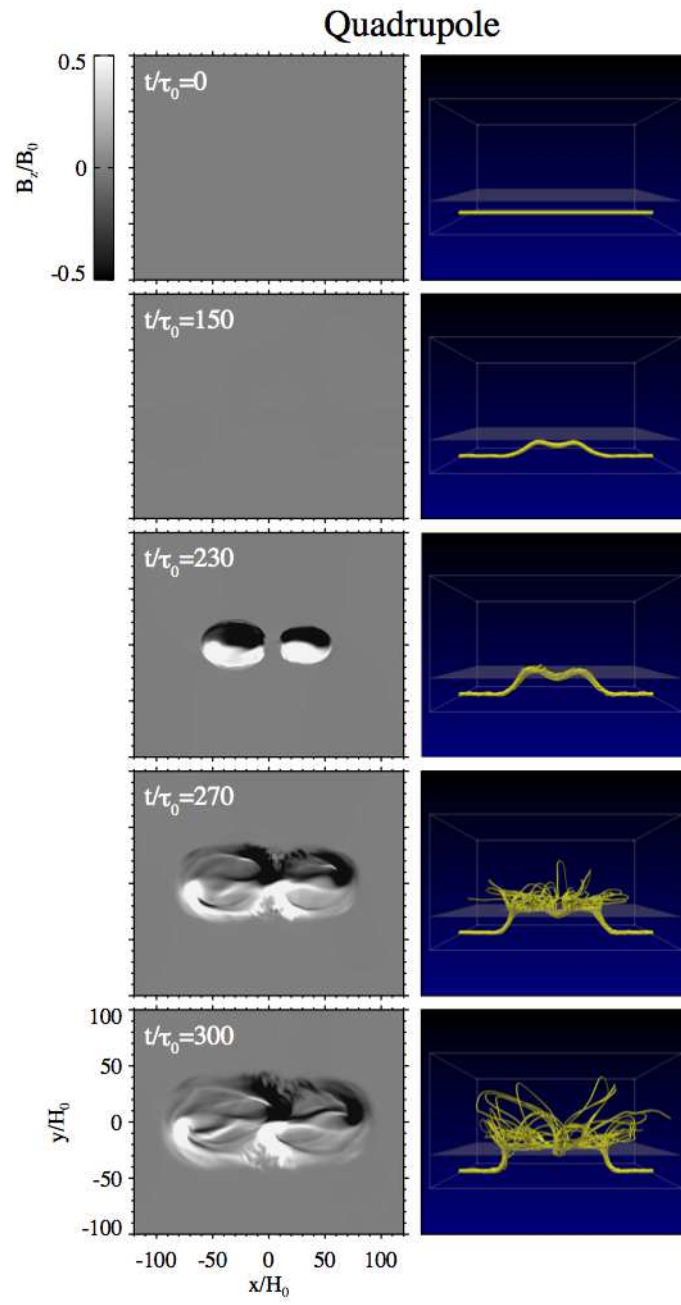


Figure 6. Same as Figure 3 but for the Quadrupole case.

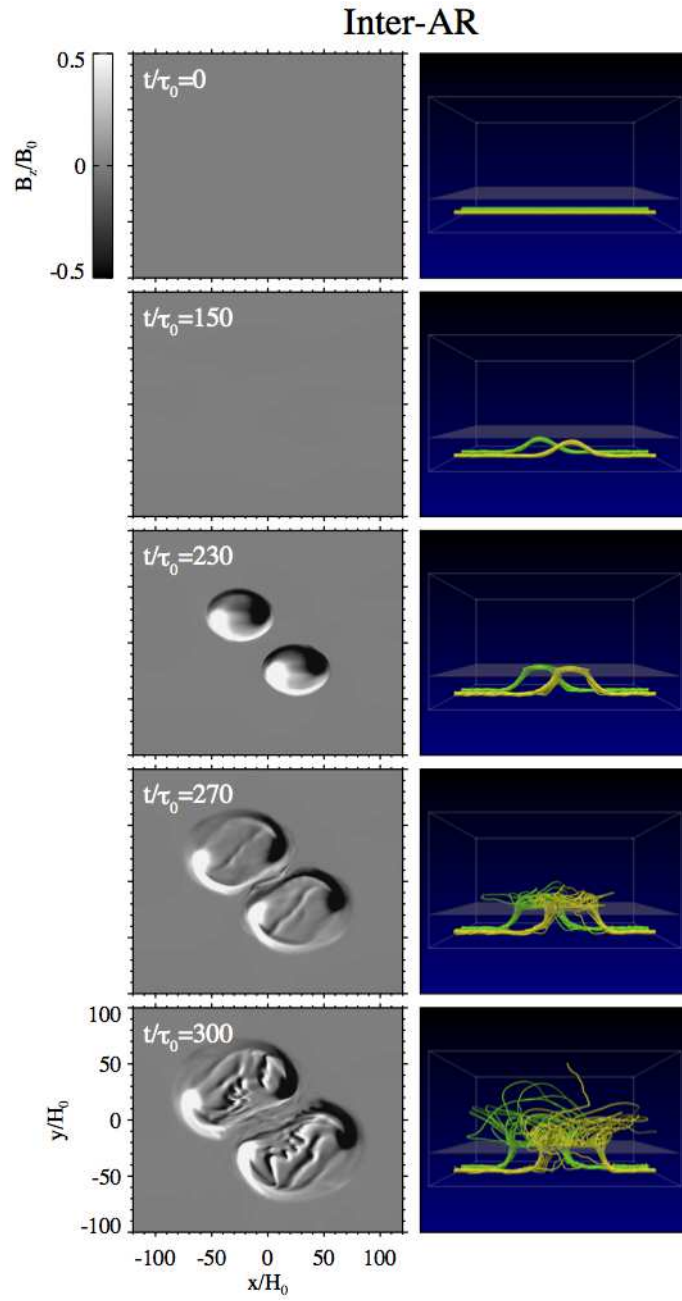


Figure 7. Same as Figure 3 but for the Inter-AR case. The green field lines are for the secondary tube.

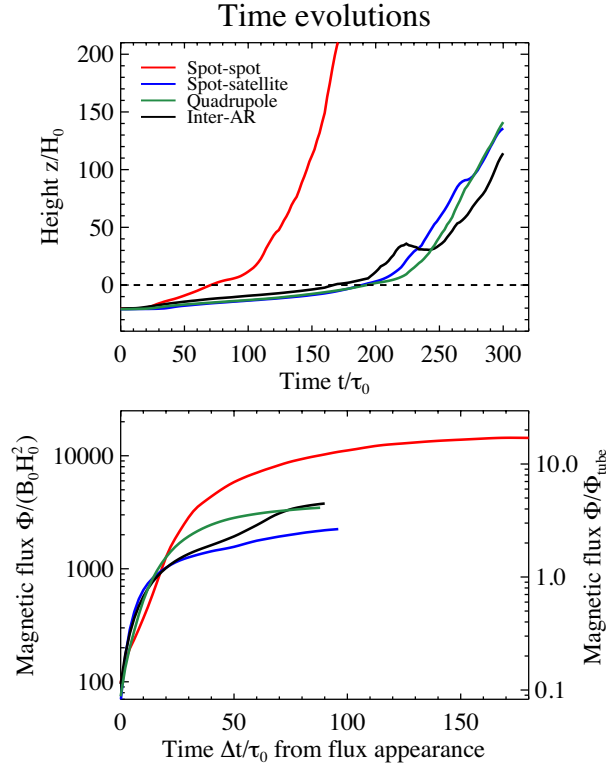


Figure 8. (Top) Time evolution of the highest part of the flux tubes for the four simulation cases. Solar surface ($z/H_0 = 0$) is indicated by a dashed line. For the Spot-Satellite case, only the contribution of the main tube is shown. (Bottom) Evolution of the total unsigned magnetic flux, $\Phi = \int |B_z| dx dy$, measured at the solar surface. Time $\Delta t/\tau_0$ is measured since the flux appears at the surface. The left vertical axis indicates the non-dimensional value of the magnetic flux, i.e., in the unit of $B_0 H_0^2$, while the right vertical axis presents the value normalized by the total axial magnetic flux of the initial flux tube, $\Phi_{\text{tube}}/(B_0 H_0^2) = 845$.

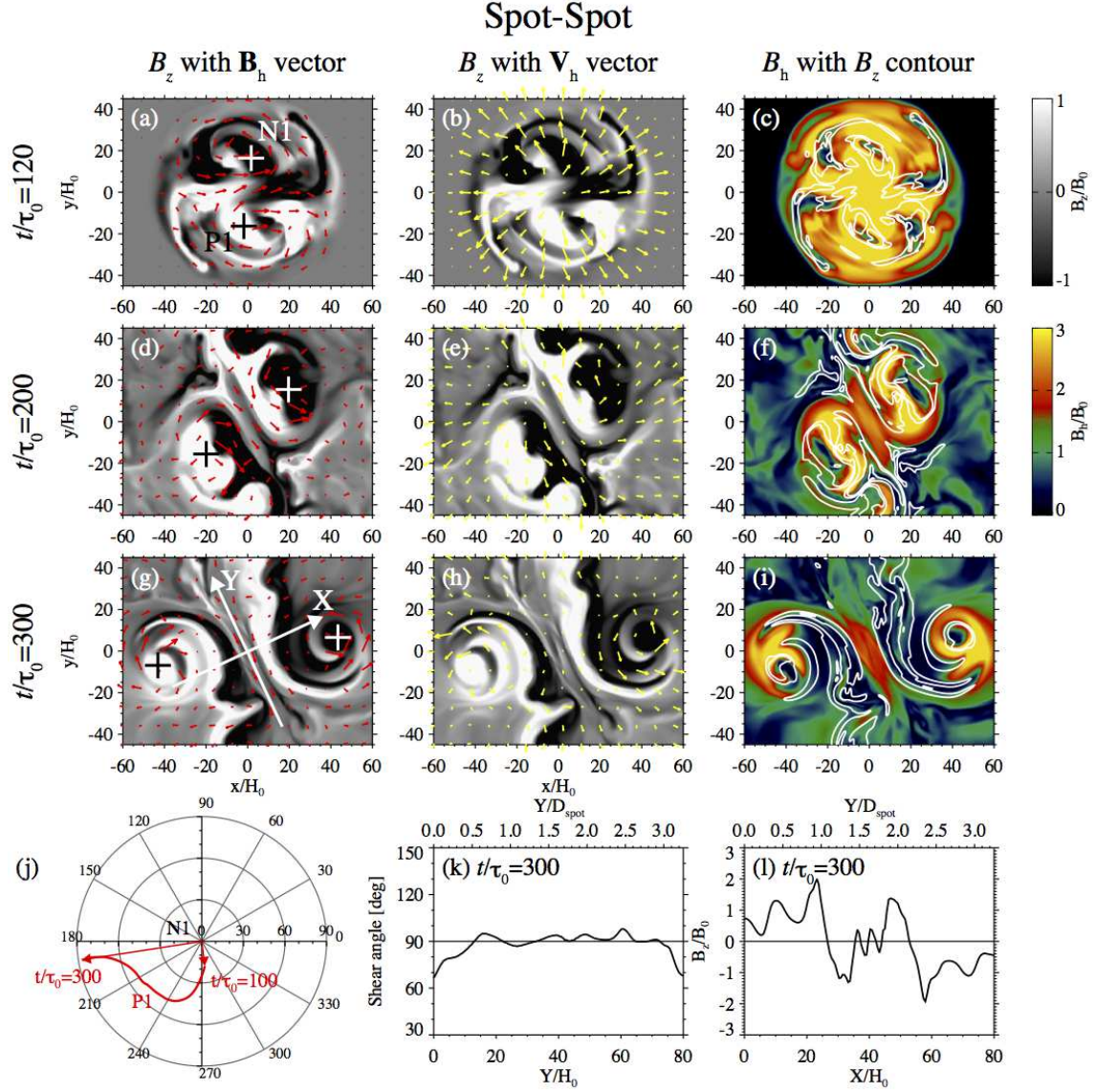


Figure 9. Formation of δ -spot and sheared PIL for the Spot-Spot case. The left column shows the magnetogram (B_z : black-white) with horizontal magnetic fields (B_h : red arrows) at three different times. Plus signs denote the centers of the two main sunspots of positive (P1) and negative (N1) polarities, which are defined as the local maximum and minimum of the vertical fields, respectively. The local coordinates (X, Y) in panel (g) are defined such that the Y -axis is parallel to the developed PIL. The horizontal velocity (V_h : yellow arrows) is shown in the middle column, while in the right column, the horizontal field strength (B_h : color) is presented. Panel (j) shows the relative motion of the sunspots N1 and P1. The center of the diagram corresponds to N1, the horizontal axis is parallel to the x -axis, and the arrow head indicates the relative position of P1. Panels (k) and (l) are the physical parameters along the X and Y axes in panel (g): the shear angle, $\arctan(B_Y/B_X)$, along the Y -axis and the vertical field, B_z/B_0 , along the X -axis. For comparison, a length scale normalized by the typical sunspot diameter, $D_{\text{spot}}/H_0 = 24.6$, is also shown as the upper horizontal axis (see main text for details).

Spot-Satellite

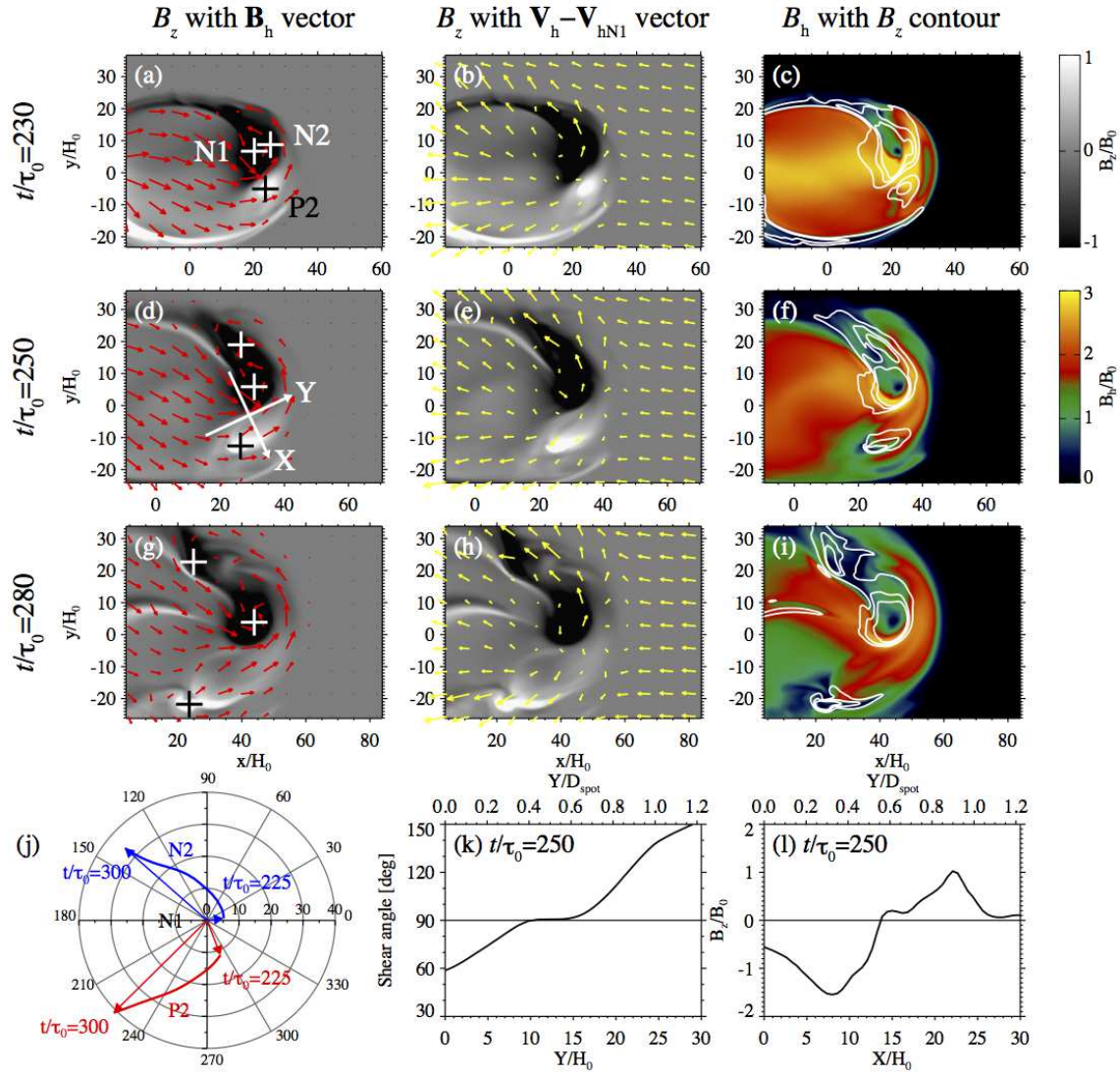


Figure 10. Same as Figure 9 but for the Spot-Satellite case. Panels (a) to (i) are shown so that the negative main polarity N1 is always located at the center of the diagram. In the middle column, the relative horizontal velocity, $\mathbf{V}_h - \mathbf{V}_{hN1}$, is plotted. In panel (j), the relative motion of N1 and N2 is also shown.

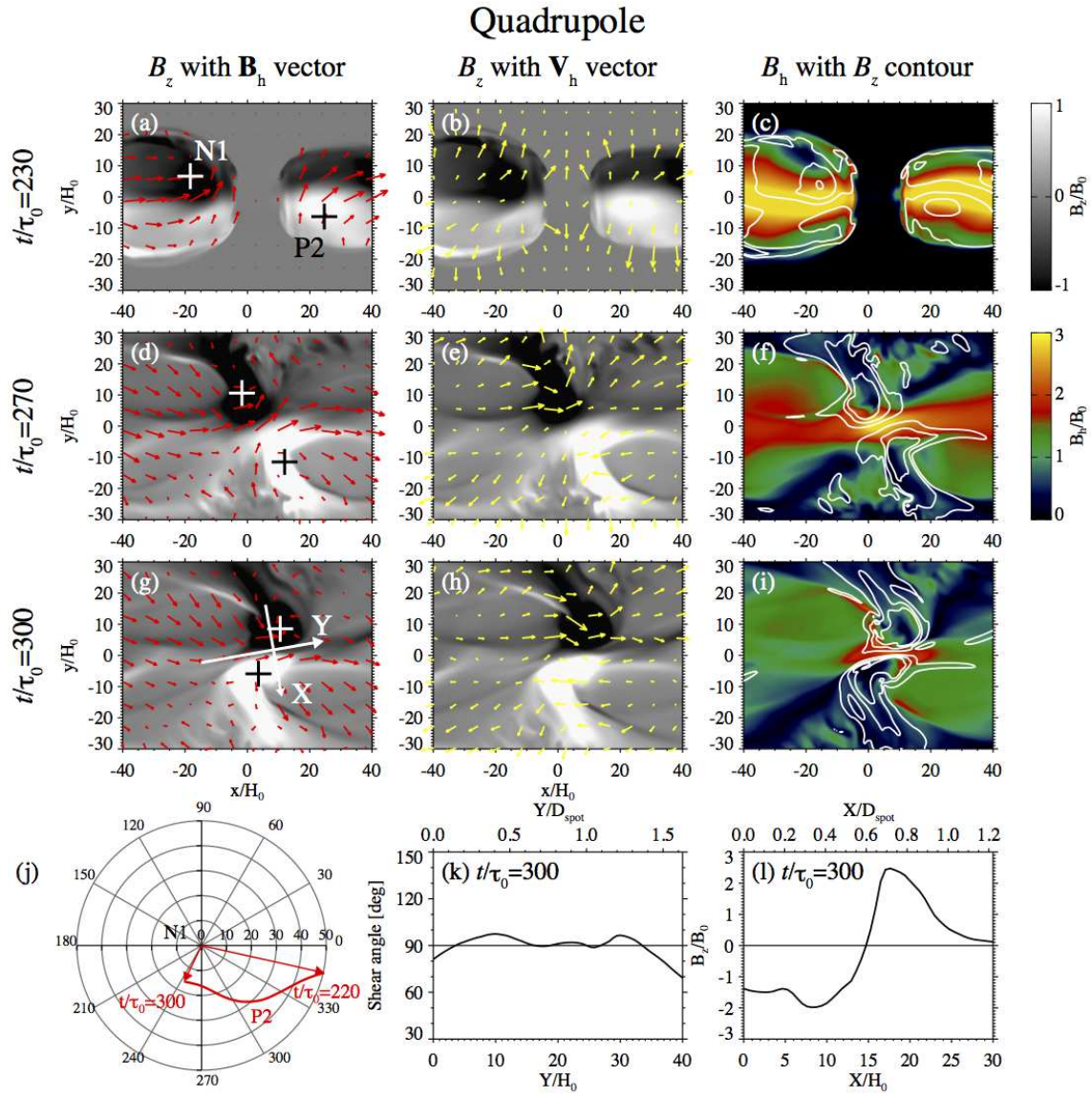


Figure 11. Same as Figure 9 but for the Quadrupole case.

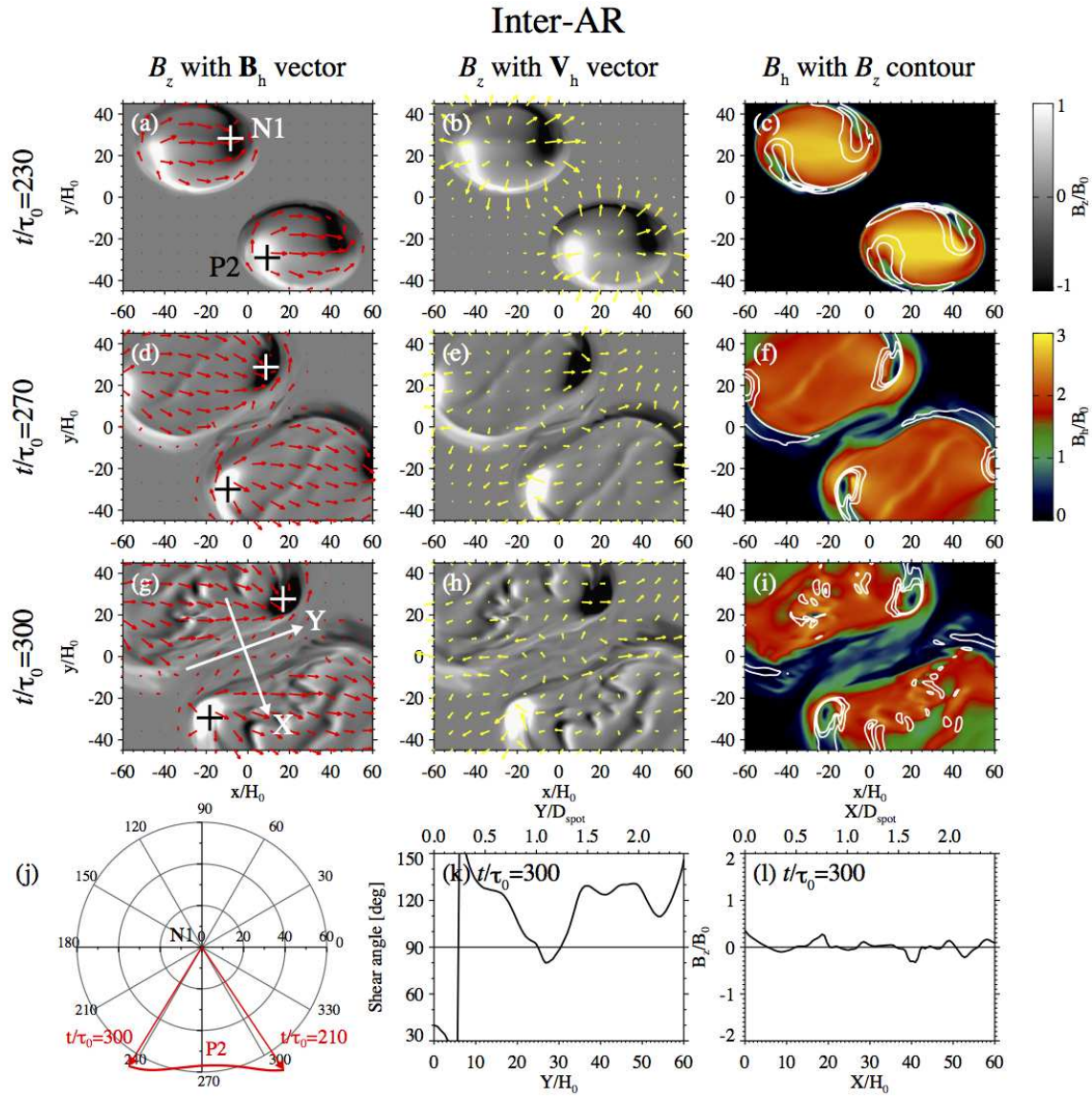


Figure 12. Same as Figure 9 but for the Inter-AR case.

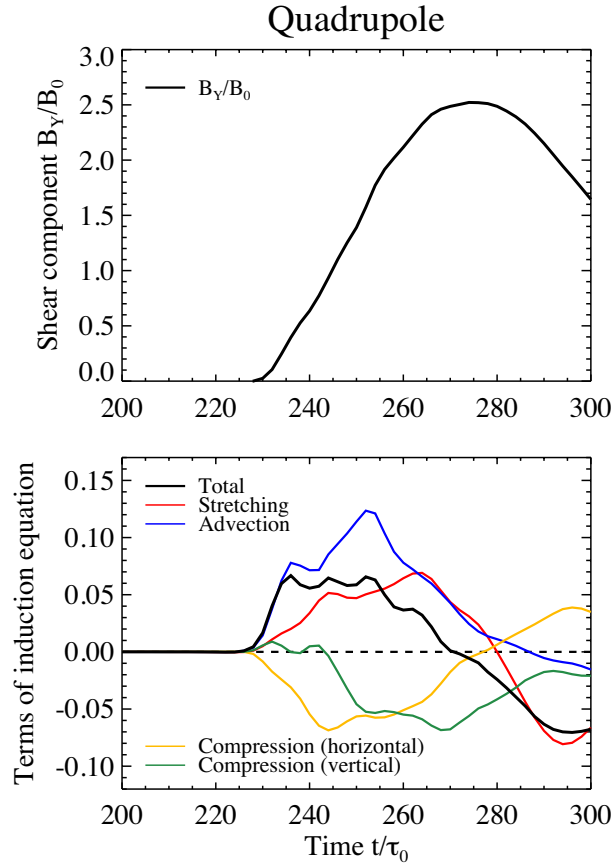


Figure 13. Evolution of the magnetic shear at the PIL of the Quadrupole case. (Top) Time evolution of the shear component B_Y/B_0 averaged over $15 \leq Y/H_0 \leq 25$, where the Y -axis is shown in Figure 11(g). (Bottom) Evolution of each term of the induction equation: see Equation (19). The zero level is indicated by a horizontal dashed line.

Field lines and current sheets

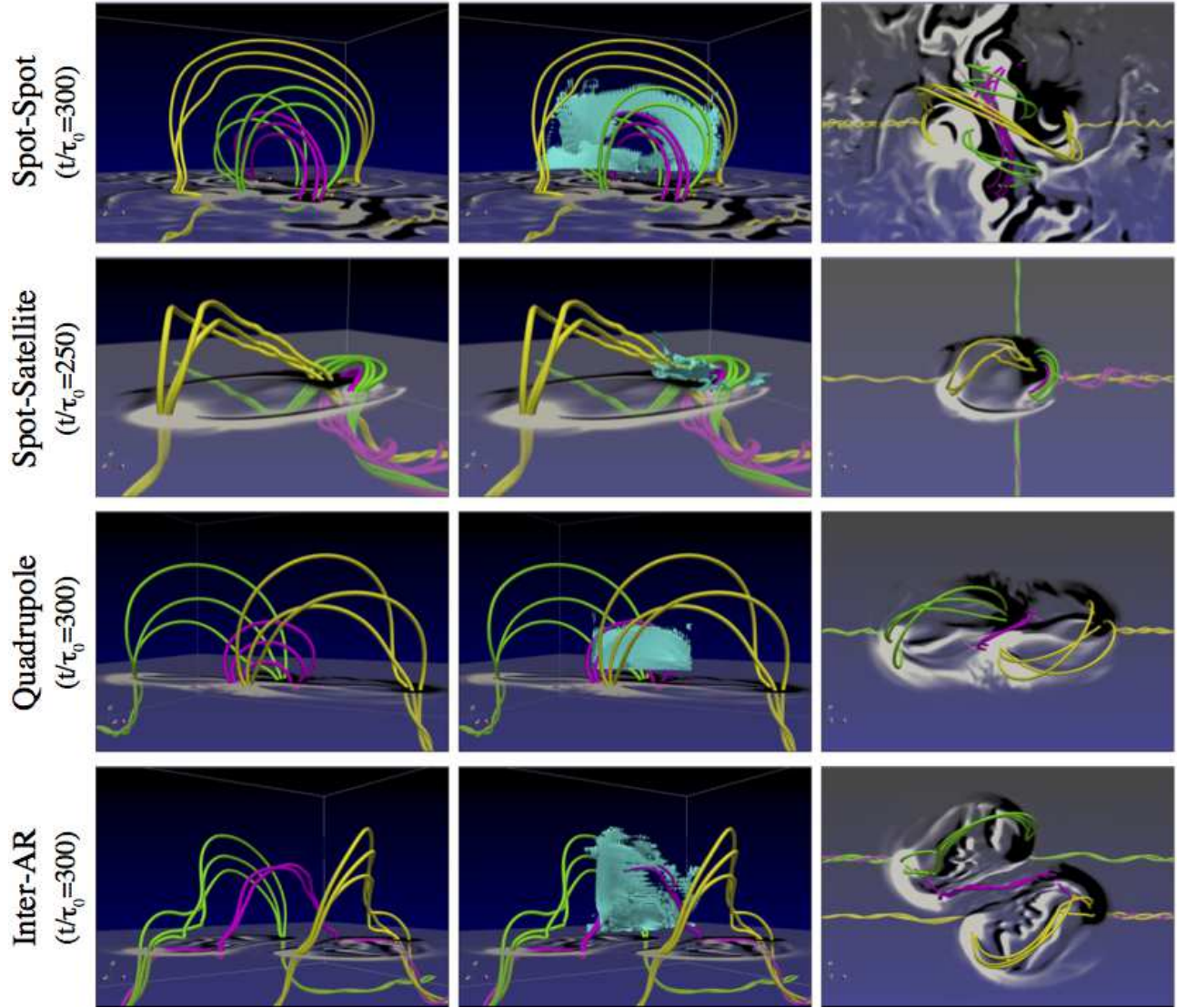


Figure 14. 3D magnetic structures for the four simulation cases. Surface magnetogram saturates at $B_z/B_0 = \pm 0.3$, with reduced transparency for weaker field regions. See main text for explanations of the colors of the field lines. In the middle column, the electric current sheets are overplotted with sky blue isocontours (see Appendix A for the definition of the current sheets).

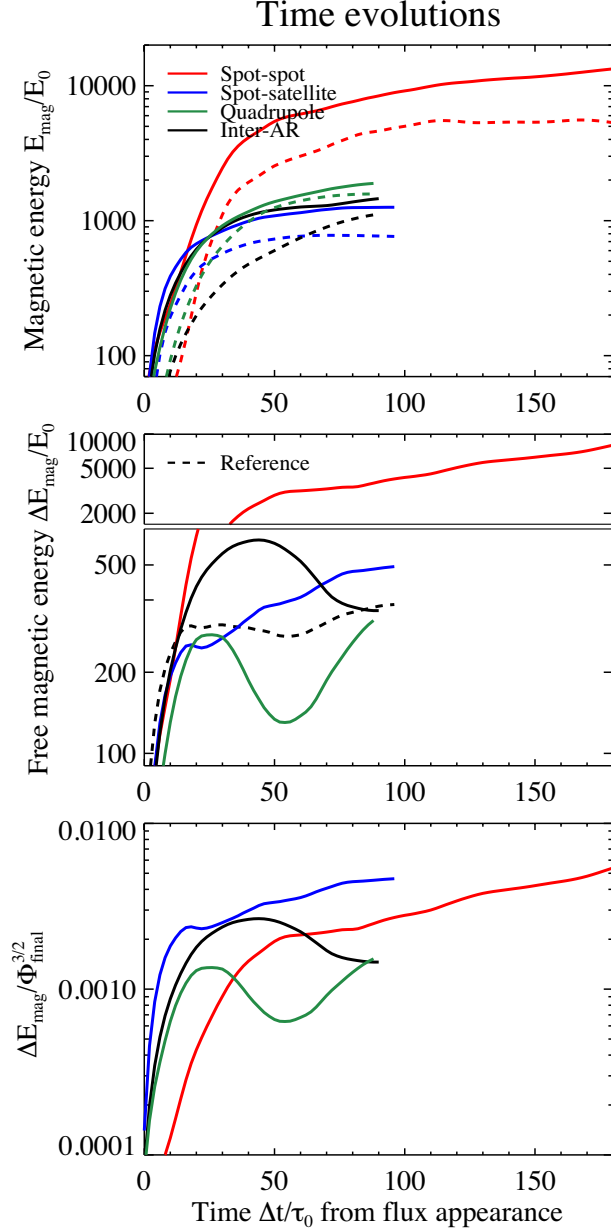


Figure 15. (Top) Time evolution of the magnetic energy in the atmosphere for the four cases. Time $\Delta t/\tau_0$ is measured since the flux appears at the surface (see Figure 8). Solid line indicates the actual total magnetic energy, E_{mag} (Equation (20)), while the dashed line is the calculated potential energy, E_{pot} (Equation (21)). (Middle) Evolution of the free magnetic energy, $\Delta E_{\text{mag}} \equiv E_{\text{mag}} - E_{\text{pot}}$. The Reference case is also plotted with a dashed line. (Bottom) Free energy normalized by the three-halves power of its final ($t/\tau_0 = 300$) photospheric unsigned magnetic flux, $\Phi_{\text{final}}^{3/2}$.

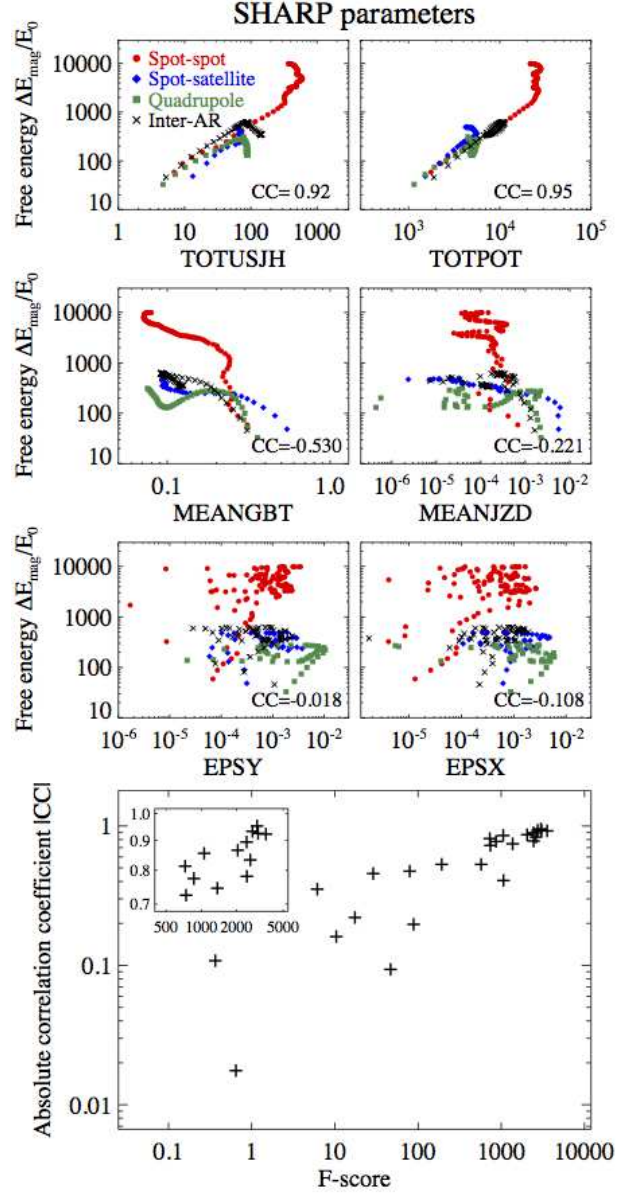


Figure 16. (Top) Six sample diagrams showing free magnetic energy $\Delta E_{\text{mag}}/E_0$ vs. SHARP parameters, which are TOTUSJH (total unsigned current helicity), TOTPOT (total photospheric magnetic free energy density), MEANGBT (mean gradient of total field), MEANJZD (mean vertical current density), EPSY (sum of y -component of normalized Lorentz force), and EPSX (sum of x -component of normalized Lorentz force); see Table 1 for detailed formulae. For the four simulations, the SHARP parameters are measured in the horizontal plane at $z_p/H_0 = 2$ with time steps of $\Delta t/\tau_0 = 2$ after the flux appears at $z_p/H_0 = 2$. Correlation coefficient, CC , calculated on the log-log plot is shown at the bottom right of each diagram. (Bottom) Scatter plot of absolute CC for all 25 SHARP parameters vs. F -score given by [Bobra & Couvidat \(2015\)](#), which indicates how well a given parameter predicts flare events.

Table 1. Properties of Flare Events

Keyword	Description	Formula	F -Score	CC	Scaling	CME Rank
TOTUSJH	Total unsigned current helicity	$H_{c_{\text{total}}} \propto \sum B_z \cdot J_z $	3560	0.922	E	16
TOTBSQ	Total magnitude of Lorentz force	$F \propto \sum B^2$	3051	0.925	E	...
TOTPOT	Total photospheric magnetic free energy density	$\rho_{\text{tot}} \propto \sum (\mathbf{B}^{\text{Obs}} - \mathbf{B}^{\text{Pot}})^2 dA$	2996	0.952	E	8
TOTUSJZ	Total unsigned vertical current	$J_{z_{\text{total}}} = \sum J_z dA$	2733	0.933	E	12
ABSNJZH	Absolute value of the net current helicity	$H_{c_{\text{abs}}} \propto \sum B_z \cdot J_z $	2618	0.833	E	13
SAVNCPP	Sum of the modulus of the net current per polarity	$J_{z_{\text{sum}}} \propto \left \sum B_z^+ J_z dA \right + \left \sum B_z^- J_z dA \right $	2448	0.781	E	18
USFLUX	Total unsigned flux	$\Phi = \sum B_z dA$	2437	0.894	E	10
AREA_ACR	Area of strong field pixels in the active region	Area = \sum Pixels	2047	0.865	E	14
TOTFZ	Sum of z -component of Lorentz force	$F_z \propto \sum (B_x^2 + B_y^2 - B_z^2) dA$	1371	0.745	E	...
MEANPOT	Mean photospheric magnetic free energy	$\bar{\rho} \propto \frac{1}{N} \sum (\mathbf{B}^{\text{Obs}} - \mathbf{B}^{\text{Pot}})^2$	1064	-0.406	I	5
R_VALUE	Sum of flux near polarity inversion line	$\Phi = \sum B_{LoS} dA$ within R mask	1057	0.855	E	15
EPSZ	Sum of z -component of normalized Lorentz force	$\delta F_z \propto \frac{\sum (B_x^2 + B_y^2 - B_z^2)}{\sum B^2}$	864.1	-0.774	I	...
SHRGT45	Fraction of Area with shear $> 45^\circ$	Area with shear $> 45^\circ$ / total area	740.8	0.725	I	7
MEANSHR	Mean shear angle	$\bar{\Gamma} = \frac{1}{N} \sum \arccos \left(\frac{\mathbf{B}^{\text{Obs}} \cdot \mathbf{B}^{\text{Pot}}}{ \mathbf{B}^{\text{Obs}} \mathbf{B}^{\text{Pot}} } \right)$	727.9	0.813	I	6
MEANGAM	Mean angle of field from radial	$\bar{\gamma} = \frac{1}{N} \sum \arctan \left(\frac{B_h}{B_z} \right)$	573.3	-0.535	I	11
MEANGBT	Mean gradient of total field	$ \nabla B_{\text{tot}} = \frac{1}{N} \sum \sqrt{\left(\frac{\partial B}{\partial x} \right)^2 + \left(\frac{\partial B}{\partial y} \right)^2}$	192.3	-0.530	I	4
MEANGBZ	Mean gradient of vertical field	$ \nabla B_z = \frac{1}{N} \sum \sqrt{\left(\frac{\partial B_z}{\partial x} \right)^2 + \left(\frac{\partial B_z}{\partial y} \right)^2}$	88.40	-0.197	I	19
MEANGBH	Mean gradient of horizontal field	$ \nabla B_h = \frac{1}{N} \sum \sqrt{\left(\frac{\partial B_h}{\partial x} \right)^2 + \left(\frac{\partial B_h}{\partial y} \right)^2}$	79.40	-0.474	I	1
MEANJZH	Mean current helicity (B_z contribution)	$\bar{H}_c \propto \frac{1}{N} \sum B_z \cdot J_z$	46.73	-0.094	I	2
TOTFY	Sum of y -component of Lorentz force	$F_y \propto \sum B_y B_z dA$	28.92	0.456	E	...
MEANJZD	Mean vertical current density	$\bar{J}_z \propto \frac{1}{N} \sum \left(\frac{\partial B_y}{\partial x} - \frac{\partial B_x}{\partial y} \right)$	17.44	-0.221	I	9
MEANALP	Mean characteristic twist parameter, α	$\alpha_{\text{total}} \propto \frac{\sum J_z \cdot B_z}{\sum B_z^2}$	10.41	-0.161	I	3
TOTFX	Sum of x -component of Lorentz force	$F_x \propto -\sum B_x B_z dA$	6.147	0.352	E	...
EPSY	Sum of y -component of normalized Lorentz force	$\delta F_y \propto \frac{-\sum B_y B_z}{\sum B^2}$	0.647	-0.018	I	...
EPSX	Sum of x -component of normalized Lorentz force	$\delta F_x \propto \frac{\sum B_x B_z}{\sum B^2}$	0.366	-0.108	I	...

NOTE—For descriptions and formulae of the SHARP parameters, we follow the original notations of [Bobra & Couvidat \(2015\)](#). In the analysis of the simulation results of this paper, we measured each parameter at the $z_p/H_0 = 2$ plane every $\Delta t/\tau_0 = 2$ after magnetic flux appears at $z_p/H_0 = 2$. The threshold for the absolute field strength above which the total and mean values are calculated is selected to be $B/B_0 = 0.04$ (equivalently 10 G), while the threshold for the “strong field” (AREA_ACR) and for measuring [Schrijver \(2007\)](#)’s R (R_VALUE) is $B/B_0 = 0.2$ (500 G). F -score here is the scoring of the parameters for predicting solar flares provided by [Bobra & Couvidat \(2015\)](#), while CC is the correlation coefficient obtained from the four simulation cases by comparing the free magnetic energy and SHARP parameter at each moment (see top panels of Figure 16). Following [Welsch et al. \(2009\)](#), we classified the parameters into extensive (E), where a given parameter increases with AR size, and intensive (I), where the parameter is independent of AR size. The rightmost column shows the ranking of features for predicting CME eruptions, as reported by [Bobra & Ionidis \(2016\)](#).